Recent Advances in Computational Methods for the Solution of the Time-Dependent Schrödinger Equation for the Interaction of Short, Intense Radiation with One and Two Electron Systems: Application to He and H_2^+

Barry I. Schneider, Johannes Feist, Stefan Nagele, Renate Pazourek, Suxing Hu, Lee A. Collins, and Joachim Burgdörfer

Abstract In the past few years new and efficient algorithms have been developed to solve the time-dependent Schrödinger equation (TDSE) for few-electron systems. When coupled with the advances in and availability of high performance computing platforms, it is now possible to numerically calculate nearly exact solutions to the interactions of short, intense laser pulses with simple one and two-electron systems. In addition, somewhat less accurate treatments of the heavier rare gases and simple two-electron molecules are also becoming available. The proceedings from this workshop have provided a unique opportunity to describe the substantial numerical

Barry I. Schneider
Office of Cyberinfrastructure and Physics Division, National Science Foundation, 4201 Wilson Blvd., Arlington, VA 22230, USA, e-mail: bschneid@nsf.gov

Johannes Feist
ITAMP, Harvard–Smithsonian Center for Astrophysics, Cambridge, MA 02138, USA, e-mail: jfeist@cfa.harvard.edu

Stefan Nagele
Institut für Theoretische Physik, Technische Universität Wien, Wiedner Hauptstraße 8, 1040 Wien, Austria, e-mail: stefan.nagele@tuwien.ac.at

Renate Pazourek
Institut für Theoretische Physik, Technische Universität Wien, Wiedner Hauptstraße 8, 1040 Wien, Austria, e-mail: renate.pazourek@tuwien.ac.at

Suxing Hu
Laboratory for Laser Energetics, University of Rochester, 250 E. River Road, PO Box 278871, Rochester, NY 14623-1212 USA, e-mail: shu@lle.rochester.edu

Lee A. Collins
Theoretical Division, Los Alamos National Laboratory, Los Alamos, NM 87545, USA, e-mail: lac@lanl.gov

Joachim Burgdörfer
Institut für Theoretische Physik, Technische Universität Wien, Wiedner Hauptstraße 8, 1040 Wien, Austria, e-mail: burg@dollywood.itp.tuwien.ac.at

A.D. Bandrauk and M. Ivanov (eds.), *Quantum Dynamic Imaging: Theoretical and Numerical Methods*, CRM Series in Mathematical Physics, DOI 10.1007/978-1-4419-9491-2_10,

and algorithmic progress that has been achieved over the past few years to solve the TDSE and to illustrate them on the He atom and H_2^+ molecule.

1 Introduction

In recent years, revolutionary new technologies have made coherent, ultrashort, and intense pulses in the vacuum and extreme ultraviolet (VUV-XUV) region available. These pulses are currently generated from two quite different types of sources.

One are free electron lasers (FEL) [1–7]. Currently, there are two FELs in the VUV-XUV and X-ray regime (XFELs) in operation: FLASH at DESY in Hamburg, Germany [8, 9], and LCLS in Stanford, USA [10, 11]. FLASH has reached focused intensities of up to $10^{16}\,\mathrm{W/cm^2}$, and photon energies as high as 190 eV, while LCLS reaches even higher energies up to 8 keV and intensities of up to $10^{18}\,\mathrm{W/cm^2}$. The duration and temporal structure of the individual FEL pulses is not well known, but is of the order of 10–50 femtoseconds for FLASH. In addition, there have been a number of proposals aimed to decrease the duration of these pulses to a few hundred attoseconds [12–18].

The other approach to produce intense ultrashort pulses at XUV wavelengths is to use high harmonic generation (HHG) from a driving infrared (IR) laser [19–28]. This technique has been successfully used to create the shortest pulses available today, with durations down to 80 as [27]. With current technology, attosecond pulses are much less intense than FEL pulses. The focused intensities are not well known but typically do not exceed $\approx 10^{12}\,\mathrm{W/cm^2}$, although various ways to increase the maximally available intensity have been proposed [29–36].

The continuing development of these novel light sources has led to an increased interest in multiphoton processes at high photon energies. Simultaneously, the ultrashort duration of the pulses in the femtosecond ($1\,\mathrm{fs} = 10^{-15}\,\mathrm{s}$) or even attosecond ($1\,\mathrm{as} = 10^{-18}\,\mathrm{s}$) domain enables the study of *time-resolved* electron dynamics, starting the field of *attosecond science* [37–41].

In this contribution, we report on some of our recent theoretical and numerical investigations, motivated by the availability of these pulses. We study relatively simple systems (He and H_2^+), for which the Schrödinger equation including all relevant degrees of freedom can be fully solved. This necessitates the use of numerical approaches that take advantage of modern high-performance computing facilities. The work that is reviewed in this manuscript has been previously published in the diploma theses of Stefan Nagele [42] and Renate Pazourek [43] and the PhD thesis of Johannes Feist [44], as well as some journal publications [45–50].

We start by giving an overview of the numerical methods we are using to discretize the spatial (Sect. 2) and temporal (Sect. 3) degrees of freedom. We then comment on some numerical details of our implementation (Sect. 4).

For the case of helium (Sect. 5), we focus on two-photon double ionization. Double ionization of helium has long been of great interest in atomic physics since it provides fundamental insights into the role of electronic correlation in the full three-

body Coulomb break-up process. This simple, two-electron system gives crucial insight into the dynamics of more complex atoms and even simple molecules [51–62]. Until recently, the focus of these studies was on one-photon double ionization, where a single photon releases both electrons from the nucleus. In two-photon double ionization (TPDI) of atomic helium, two electrons are absorbed either simultaneously or sequentially, ejecting both electrons. This is one of the simplest multiphoton processes involving electron correlation, and has been the subject of intense studies in the past few years [42–49, 63–114]. We discuss both (i) cross sections in the *nonsequential* regime of TPDI, which require pulses of at least a few femtoseconds duration, and (ii) the possibility to probe and control correlation using ultrashort (attosecond) XUV pulses in the *sequential* regime of TPDI.

In Sect. 6, we then discuss the hydrogen molecular ion H_2^+. We simulate its combined electronic and nuclear motion in attosecond pulses fully, i.e., without resorting to the Born–Oppenheimer approximation. We study energy and angular patterns in one-photon ionization. The conclusions we draw for this simple test case could be applied to e.g., attosecond photoelectron microscopy. The photoelectron distribution obtained through ionization by an attosecond pulse can provide information about the "frozen" position of the (slowly moving) nuclei after excitation through other means. We demonstrate a strong polarization dependence for the ionization probability, which disappears for high photon energies ($\gtrsim 170\,\mathrm{eV}$). In addition, we find that the double slit interference pattern that is caused by the two distinct molecular centers in the half-scattering process of photoionization only follows the classical Young's double slit angular distribution if the electron de Broglie wavelength is noticeably smaller than the internuclear distance.

2 An Introduction to the Finite Element Discrete Variable Representation (FEDVR)

To solve the multidimensional, time-dependent Schrödinger equation,

$$\mathrm{i}\hbar\frac{\partial}{\partial t}|\Psi(t)\rangle = \widehat{\mathbf{H}}|\Psi(t)\rangle \ , \tag{1}$$

one requires an efficient spatial discretization approach, and a way to couple that to a time-propagation technique that can exploit the structure of that discretization. Finite difference methods offer great simplicity and have been used for decades to numerically solve a variety of problems involving partial differential equations in science and engineering. However, approximating derivatives by finite difference formulas is intrinsically inaccurate unless high order methods are employed. In recent years, an alternative approach, the FEDVR, has been developed [115–118], which offers the accuracy of a spectral method and much of the simplicity and sparsity of finite difference approaches. This approach, which we describe in some detail

below, employs the standard finite element method, but replaces the usual polynomial basis in each element by a basis derived from a discrete variable representation.

2.1 *Finite Elements*

The basic idea of any *finite element* (FE) method is to divide the underlying configuration space of a (partial) differential equation into small subdomains or finite elements. For complex geometries in more than one dimension, FE techniques are especially useful to handle the boundary conditions that need to be satisfied at the surface or internally for the equation under consideration. However, they are also useful for "simple" problems in one dimension. In that case, each variable is divided into segments or finite elements with the FE boundaries

$$0 \leq x^{(1)} < x^{(2)} < \cdots < x^{(N)} \leq x_{max} \ . \tag{2}$$

The approach of the FEDVR is to expand the wave function in a basis of functions that are local to each finite element,

$$f_m^{(i)}(x) \ , x \in [x^{(i)}, x^{(i+1)}] \ . \tag{3}$$

The basis in a given element is *defined* to be zero outside of that element. The only remaining issue is how the basis functions at the edges of each element connect with adjacent elements. Since the equations under consideration contain at most second order spatial derivatives, it is sufficient to ensure function continuity at the edges of the boundary elements from a rigorous mathematical treatment [119]. This does not mean that adding additional constraints on the basis functions such as first or second derivative continuity would not produce a more accurate representation for a fixed number of basis functions, it is just not required and by only imposing basis function continuity, the problem is significantly easier to handle numerically. In each finite element, we choose basis functions obtained from a *discrete variable representation* (DVR) approach, which also provides a prescription for calculating matrix elements. Apart from the basic idea of splitting space into smaller elements, we do not use the further features of FE methods. A more detailed treatment of the subject can be found in, e.g., [120].

2.2 *Discrete Variable Representation*

In this section we provide a self-contained introduction (following [121–124]) to the polynomial *discrete variable representation* (DVR), which is closely related to the well-known concept of the spectral (finite-basis) representation of wave functions. In coordinate space a wave function in its *spectral representation* (SR)

$$\langle x|\Psi\rangle = \sum_{m=1}^{N} \langle x|\Phi_m\rangle\langle\Phi_m|\Psi\rangle = \sum_{m=1}^{N} a_m \langle x|\Phi_m\rangle \tag{4}$$

is described by the expansion coefficients

$$a_m = \langle\Phi_m|\Psi\rangle = \int \langle\Phi_m|x\rangle\langle x|\Psi\rangle \mathrm{d}x \tag{5}$$

in a given orthonormalized basis $\{|\Phi_m\rangle\}$ of the Hilbert space, where usually the basis is complete for $N \to \infty$. For $N \neq \infty$, this representation is also called a *finite basis representation* (FBR). The basis functions are orthonormal and thus fulfill

$$\langle\Phi_m|\Phi_n\rangle = \int \langle\Phi_m|x\rangle\langle x|\Phi_n\rangle \mathrm{d}x = \delta_{mn} \ . \tag{6}$$

Inserting this ansatz for the wave function in the time-independent Schrödinger equation gives

$$\sum_{m=1}^{N} \langle\Phi_n|\widehat{\mathbf{H}}|\Phi_m\rangle a_m = \sum_{m=1}^{N} \widehat{\mathbf{H}}_{nm} a_m = a_n E \ , \tag{7}$$

which is a matrix eigenvalue problem once the matrix elements $\widehat{\mathbf{H}}_{nm} = \langle\Phi_n|\widehat{\mathbf{H}}|\Phi_m\rangle$ have been calculated. Equation (7) may be derived from the Rayleigh-Ritz variational principle. The coefficients a_n can be understood as the variational parameters resulting from the application of that principle to the Schrödinger equation. As a consequence the eigenvalues (7) will always represent an upper bound to the true solution for $N \to \infty$. Thus, the SR is sometimes also called *variational basis representation* (VBR).

The idea behind the DVR is to start by choosing a basis $\{|\Phi_m\rangle\}$ for which the overlap integrals in (6) can be evaluated *exactly* by numerical quadrature. The classical orthogonal polynomials up to order $N-1$ are such a set. For each of these basis sets, there is an associated Gaussian quadrature of order N in which the product of two of these functions can be integrated exactly. This arises simply because the product is itself a polynomial of maximum order $2N-2$ which may be integrated exactly by an Nth-order Gaussian quadrature at points x_i with weights w_i. Replacing the integral in (5) by its discrete approximation yields

$$\tilde{a}_m = \sum_{j=1}^{N} w_j \langle\Phi_m|x_j\rangle\langle x_j|\Psi\rangle \tag{8}$$

with the FBR remaining orthonormal under the quadrature rule,

$$\langle\Phi_m|\Phi_n\rangle = \sum_{j=1}^{N} w_j \langle\Phi_m|x_j\rangle\langle x_j|\Phi_n\rangle = \delta_{mn} \ . \tag{9}$$

At this point, the only approximation that has been made is the use of the FBR. What we have not yet specified is how the matrix elements $\langle \Phi_n | \widehat{\mathbf{H}} | \Phi_m \rangle$ will be calculated. It is straightforward to show that it is possible to compute the matrix elements of the kinetic energy operators exactly for most, if not all, of the classical orthogonal functions. However, the matrix elements of the potential are another matter. These are often complex functions of x and all that can be said is that using the quadrature rule for the matrix elements,

$$\langle \Phi_m | \widehat{\mathbf{V}} | \Phi_n \rangle = \int \Phi_m^*(x) V(x) \Phi_n(x) \mathrm{d}x \simeq \sum_j^N w_j \Phi_m^*(x_j) V(x_j) \Phi_n(x_j) \ , \qquad (10)$$

needs to be examined for accuracy. There is another disadvantage of (10). It is not diagonal in the FBR basis. While this is not terribly serious for a one-dimensional problem, it still would be nice if one could find an approach which only required the value of the potential at the i^{th} quadrature point. Such a diagonal representation, suitably generalized to the multidimensional case, could have very large advantages in practical computations. Provided that the quadrature approximation is accurate, it is possible to make a basis set transformation which does render the potential diagonal in the transformed basis. This new basis, $\{f_j(x)\}$, the DVR basis, has the property that the basis functions are zero at all but one quadrature point, i.e.,

$$f_j(x_i) = \frac{\delta_{ij}}{\sqrt{w_i}} \qquad (11)$$

and in analogy to (4) and (9) they define an orthonormal basis (a rigorous proof can be found in [121]),

$$\langle f_i | f_j \rangle = \int f_i^*(x) f_j(x) \mathrm{d}x \stackrel{!}{=} \sum_{m=1}^N w_m f_i^*(x_m) f_j(x_m) = \delta_{ij} \ . \qquad (12)$$

The wave function (4) then reads

$$\langle x | \Psi \rangle = \sum_{m=1}^N \tilde{a}_m \langle x | \Phi_m \rangle \simeq \sum_{m=1}^N \sum_{j=1}^N w_j \langle x | \Phi_m \rangle \langle \Phi_m | x_j \rangle \langle x_j | \Psi \rangle \ . \qquad (13)$$

The DVR basis functions can be obtained from,

$$f_j(x) = \sqrt{w_j} \sum_{m=1}^N \langle x | \Phi_m \rangle \langle \Phi_m | x_j \rangle \ . \qquad (14)$$

The wave function is then expressed as,

$$\langle x | \Psi \rangle = \sum_{j=1}^N \langle x | f_j \rangle \langle f_j | \Psi \rangle = \sum_{j=1}^N \tilde{\Psi}_j f_j(x) \ , \qquad (15)$$

where the coefficients $\tilde{\Psi}_j = \langle f_j|\Psi\rangle$ are also directly connected to the values of the wave function at the grid points, $\tilde{\Psi}_j = \sqrt{w_j}\Psi(x_j)$. This is the reason that the DVR can be seen as a bridge between spectral basis methods and grid-based approaches – the coefficients of the basis functions f_j simultaneously give the values of the wave function at the grid points in coordinate space, which are chosen as the quadrature points of the underlying Gaussian quadrature.

A further consequence of this is that the coordinate operator is strictly diagonal in the DVR basis,

$$\langle f_i|\hat{x}|f_j\rangle = \delta_{ij}x_i \ , \tag{16}$$

as the product of two basis functions has maximum order $2N-2$ and integrals up to order $2N-1$ can be evaluated exactly by N-point Gaussian quadrature. Consequently, the functions $f_j(x)$ can be referred to as *coordinate eigenfunctions* because they depend only on the chosen quadrature and the corresponding mesh (which are, in turn, related to the corresponding equivalent finite-basis representation).

In a DVR, the wave functions are thus represented by a complete and orthonormal set of basis functions that are uniquely related to the chosen grid and quadrature. The FBR and DVR are strictly equivalent (*isomorphic*) if the FBR consists of orthogonal polynomials, as we have chosen here [125, 126].

A DVR basis function is effectively represented by an *interpolating polynomial*. For a given order this interpolating polynomial is unique [127] and we can express it without loss of generality by the Lagrange polynomials,

$$L_i(x) = \prod_{j\neq i}\frac{x-x_j}{x_i-x_j} \tag{17}$$

which fulfill

$$L_i(x_j) = \delta_{ij} \ . \tag{18}$$

As the representation is unique, i.e., the Lagrange polynomials form the only polynomial basis that fulfills (18), they are identical to the basis functions $f_j(x)$ (up to a factor $\sqrt{w_j}$). This is the reason why in many publications (following a series of papers by Baye et al. [128–130]) polynomial DVRs are referred to as Lagrange-mesh techniques. Last, but certainly not least, in the DVR, the potential matrix elements are diagonal ((11) and (16)) within the accuracy of the quadrature approximation,

$$\langle f_i|\widehat{\mathbf{V}}|f_j\rangle \overset{!}{\simeq} V(x_i)\delta_{ij} \tag{19}$$

and thus equal to the potential evaluated at the grid points. This does not imply that the potential matrix elements are calculated *exactly* by quadrature. The reason is that a N-point Gaussian quadrature just allows for an exact calculation of polynomial integrands of degree $2N-1$ and the required matrix element will not, in general, posses that property. In practice, it has been found that for sufficiently large N, the use of the DVR rule (19) works well. Stated differently, the *fundamental approximation* of the DVR is that all matrix elements of coordinate operators are diagonal. In other words (referring to the isomorphic FBR) the quadrature is not exact

for those components of $\widehat{\mathbf{V}}|\Phi_i\rangle$ (*aliasing terms*) that do not remain in the spectral basis [131]. In practice, those errors are removed *implicitly* by extending the basis size until numerical convergence is reached. However, the strict variational properties of (7) are lost in the DVR. A more detailed treatment of the problem is given in [125, 131].

2.2.1 Calculating Derivatives

In the DVR basis the n-th derivative of a function $\Psi(x)$ is given by

$$\frac{\partial^n \Psi}{\partial x^n}(x) = \sum_{j=1}^{N} \tilde{\Psi}_j \frac{\partial^n f_j}{\partial x^n}(x) \,, \tag{20}$$

where the derivatives of the basis functions $\frac{\partial^n f_j(x)}{\partial x^n}$ have to be computed just once initially. If the n-th derivative is to be evaluated at the DVR points one gets

$$\frac{\partial^n \Psi}{\partial x^n}(x_i) = \sum_{j=1}^{N} \frac{\partial^n f_j}{\partial x^n}(x_i)\sqrt{\omega_i}\tilde{\Psi}_j := D_{ij}\tilde{\Psi}_j \tag{21}$$

which represents a matrix-vector multiplication. Thus, in a DVR basis derivatives are calculated by multiplying the vectors $\tilde{\Psi}_j$ by a differentiation matrix $\mathbf{D}$. The matrix $\mathbf{D}$ is full and hence the matrix-vector product is computationally expensive when the basis size is large.

2.3 *FEDVR*

In an FEDVR [115–118] the underlying configuration space of a problem is divided into elements in each of which the wave function is represented in a local DVR basis. Consequently, the main advantages of the two techniques are brought together:

- Since the DVR basis functions are only defined on *local* grids, the kinetic energy matrix is not full as in the standard DVR approach (cf. (20)) but consists of several blocks (one for each FE) which overlap at only one point (see Fig. 1). Thus, the matrix becomes quite sparse in 1D. Matrix-vector products can be calculated efficiently when a direct product basis is used in N dimensions. This property also allows for a computationally efficient *parallelization* scheme in which the inherent latency due to communication between the matrix blocks is minimal. As long as the number of basis functions in a given element is not too small compared to the size of the element, this provides an accurate numerical expression for the derivatives [115].
- For a local potential, the matrix is diagonal, thus avoiding the need to calculate complex matrix elements as in SR or FBR methods.

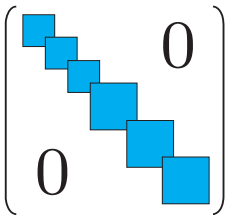

Fig. 1 Illustration of the block structure of the kinetic energy operator of the FEDVR in one dimension.

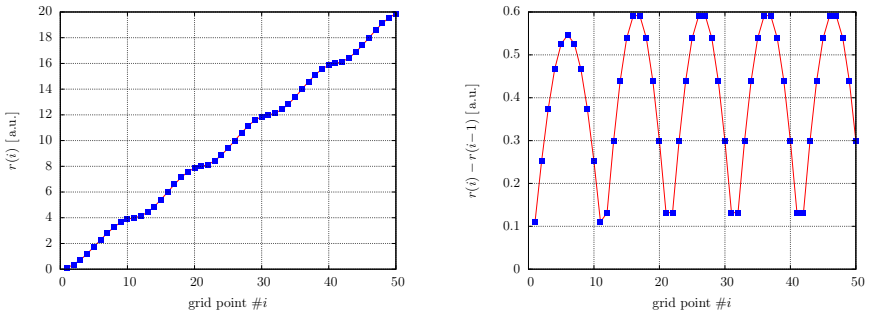

(a) Grid point distribution (b) Grid point spacing

Fig. 2 Mesh points of a typical FEDVR grid with eleven basis functions per finite element. The oscillatory structure in the grid spacing is a consequence of the Gauss–Lobatto quadrature.

Since the resulting grid is composed of many local sub-grids for each finite element we have to use a quadrature where the end point in each node coincides with the starting point for the neighboring finite element. This is necessary to impose continuity for the represented wave functions. For Gauss-Legendre quadratures the mesh points are given by the roots of the Legendre polynomials. As all these roots lie *inside* the sub-grids, we instead use a Gauss–Lobatto quadrature in each element. In a Gauss–Lobatto quadrature, the first and last points are explicitly chosen, which leads to a slightly reduced accuracy. By choosing the first and last points to lie exactly at the FE boundaries, we can connect the last basis function in each element with the first function in the following element, forming a "bridge" function. By employing a Gaussian quadrature we implicitly choose a polynomial basis in the equivalent SR.

Figure 2 shows the first points of a typical FEDVR grid with eleven basis functions per finite element and the resulting grid spacing. The finite elements have a constant extension of 4 a.u.. The FEDVR parameters determine the maximum energy of electrons that can be well represented on the grid, which is around 6 a.u. for the parameters used here. Near the origin, the basis has to represent the Coulomb singularity of the nuclear potential, which is already done with good accuracy for the parameters given here (the ground-state energy of the one-particle Hamiltonian has a relative error of $\approx 10^{-8}$). In order to increase the accuracy, it would be possible to use smaller finite elements close to the origin.

From a Lagrange basis for each element

$$L_m^{(i)}(r) := \begin{cases} \prod_{j \neq m} \frac{r - r_j^{(i)}}{r_m^{(i)} - r_j^{(i)}} & r^{(i)} \leq r \leq r^{(i+1)}, 1 \leq i \leq N \\ 0 & \text{else} \end{cases} \tag{22}$$

we thus obtain (in agreement with [115]) the normalized FEDVR basis functions

$$f_m^{(i)}(r) := \begin{cases} \frac{L_1^{(i)}(r) + L_{M_i}^{(i-1)}(r)}{\sqrt{w_1^{(i)} + w_{M_i}^{(i-1)}}} & m = 1 \\ \frac{L_m^{(i)}(r)}{\sqrt{w_m^{(i)}}} & m = 2, \ldots, M_i - 1 \\ \frac{L_{M_i}^{(i)}(r) + L_1^{(i+1)}(r)}{\sqrt{w_{M_i}^{(i)} + w_1^{(i+1)}}} & m = M_i \end{cases} \tag{23}$$

which fulfill the orthonormality relation

$$\begin{aligned} \langle f_m^{(i)} | f_n^{(j)} \rangle &= \int f_m^{(i)^*}(r) f_n^{(j)}(r) \, \mathrm{d}r \\ &\overset{!}{\simeq} \sum_{l=1}^{N} \sum_{k=1}^{M_i} w_k^{(l)} f_m^{(i)^*}(r_k^{(l)}) f_n^{(j)}(r_k^{(l)}) = \delta_{ij} \delta_{mn} \, . \end{aligned} \tag{24}$$

In contrast to (12), the FEDVR basis functions are only approximately orthogonal because for each element the integrand in (24) is a polynomial of degree $2M_i - 2$ whereas the integration is only exact for polynomials up to degree $2M_i - 3$. This deficiency of FEDVR compared to the DVR has little effect in practice since it can be compensated by increasing the number of basis functions.

The definitions for the *bridge functions* (at $m = 1$ and $m = M_i$) in (23) ensure that $f_{M_i}^{(i)}(r) = f_1^{(i+1)}(r)$ and thus the continuity of the represented wave functions at the FE boundaries. In contrast, the first derivative is not continuous, since the finite elements have an overlap of only one grid point. As pointed out in [119] the matrix elements of the momentum operator (which is equivalent to the derivative operator) and the kinetic energy operator (which relies on the calculation of the second derivative) are nevertheless correctly defined. The integrals $\langle f_m^{(i)} | \mathrm{d}/\mathrm{d}r | f_n^{(j)} \rangle$ for the first derivative operator can be directly calculated, while the second derivative integrals need to be performed by partial integration, such that only first derivatives remain to be evaluated.

In analogy to (15) a wave function $\Psi(r)$ can be written as

$$\Psi(r) = \sum_{j=1}^{N} \sum_{k=1}^{M_j} \tilde{\Psi}_k^{(j)} f_k^{(j)}(r) \tag{25}$$

and the scalar product of two wave functions in FEDVR representation is given by

$$\langle\varphi|\psi\rangle = \sum_{i,k} \tilde{\varphi}_k^{(i)*} f_k^{(i)*}(r) \sum_{j,l} \tilde{\psi}_l^{(j)} f_l^{(j)}(r) \quad \mathrm{d}r \simeq \sum_{i,k} \tilde{\varphi}_k^{(i)*} \tilde{\psi}_k^{(i)} \ . \tag{26}$$

Consequently also the potential matrix elements are approximately diagonal, cf. (19)

$$\langle f_m^{(i)}|\widehat{\mathbf{V}}|f_n^{(j)}\rangle \overset{!}{\simeq} V\left(r_m^{(i)}\right)\delta_{ij}\delta_{mn} \tag{27}$$

and derivatives are calculated by deriving the basis functions, cf. (20)

$$\frac{\partial^n \Psi(r)}{\partial r^n} = \sum_{j=1}^{N} \sum_{k=1}^{M_j} \tilde{\Psi}_k^{(j)} \frac{\partial^n f_k^{(j)}(r)}{\partial r^n} \ . \tag{28}$$

Figure 3 shows the eigenvalues of the *discrete* Laplace operator on a FEDVR grid as obtained from (28). The step-like behavior for higher eigenvalues is a consequence of the division into finite elements. For physical problems one has to ensure that the occurring energies are in the region where the eigenvalues grow quadratically (and mimic the dispersion relation of a free particle).

2.3.1 Boundary Conditions

The FEDVR method, as outlined above, provides a flexible and accurate way of discretizing differential equations. In addition it is also necessary to properly implement the boundary conditions. How to accomplish this is a function of the coordinate under consideration. For example, in spherical coordinates, the wave function must behave regularly at the left hand boundary or matrix elements of potentials

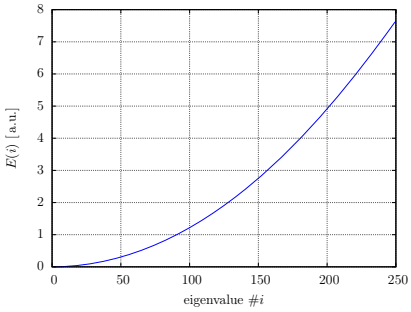

(a) The first eigenenergies of a FEDVR grid grow quadratically.

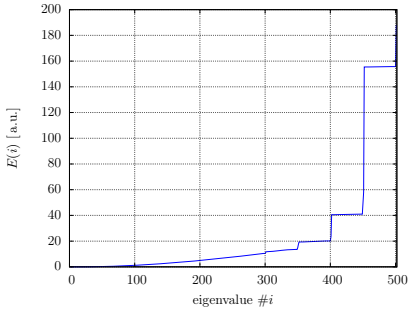

(b) For higher energies the spectrum contains "unphysical" steps due to the division into finite elements.

Fig. 3 Eigenvalues of the *discrete* Laplace operator on a FEDVR grid with $r_{\max} = 200$ a.u. and eleven basis functions per finite element. The finite elements have an extension of 4 a.u.. The resulting number of grid points is 501.

such as the Coulomb potential will diverge. One way to ensure that this behavior is satisfied is to omit the first basis function from the DVR wave-function expansion. By keeping the last basis function at the right hand boundary, one may impose open boundary conditions on the wave function. If the last basis function is removed from the expansion, this is tantamount to requiring the wave function to vanish at the right most boundary. If a wave packet reaches $r_{\max}$ during propagation, it encounters "hard walls" in any case since $\Psi(r > r_{\max}) = 0$ is imposed implicitly due to the end of the grid. The resulting unphysical reflections have to be avoided by either extending the grid so that the boundary is never reached in computing any physically meaningful quantities or by implementing *absorbing boundaries* (see following section).

3 Temporal Discretization

With the help of the time evolution operator

$$\widehat{\mathbf{U}}(t + \Delta t, t) = \mathcal{T} \exp\left(-\mathrm{i} \int_t^{t+\Delta t} \widehat{\mathbf{H}}(t')\, \mathrm{d}t'\right) \tag{29}$$

the solution of the TDSE for a given initial state $|\Psi(t_0)\rangle$ can formally be written as

$$|\Psi(t_0 + \Delta t)\rangle = \widehat{\mathbf{U}}(t_0 + \Delta t, t_0)|\Psi(t_0)\rangle = \mathcal{T} \exp\left(-\mathrm{i} \int_{t_0}^{t_0+\Delta t} \widehat{\mathbf{H}}(t')\, \mathrm{d}t'\right)|\Psi(t_0)\rangle \tag{30}$$

where $\mathcal{T}$ denotes the time-ordering operator for the exponential with noncommuting argument ($[\widehat{\mathbf{H}}(t_1), \widehat{\mathbf{H}}(t_2)] \neq 0$).

Direct evaluation of (30) is cumbersome since the time evolution operator has to be expanded in a Dyson series to represent the time-ordering. However, for small time intervals Δt the Hamiltonian can be assumed to be constant, thus giving

$$\widehat{\mathbf{U}}(t + \Delta t, t) \simeq \exp(-\mathrm{i}\widehat{\mathbf{H}}(t)\Delta t) \tag{31}$$

and

$$|\Psi(t + \Delta t)\rangle \simeq \exp(-\mathrm{i}\widehat{\mathbf{H}}(t)\Delta t)|\Psi(t)\rangle\ . \tag{32}$$

The time evolution operator (29) is *transitive*

$$\widehat{\mathbf{U}}(t + 2\Delta t, t) = \widehat{\mathbf{U}}(t + 2\Delta t, t + \Delta t)\widehat{\mathbf{U}}(t + \Delta t, t) \tag{33}$$

and *unitary*

$$\begin{aligned} &\widehat{\mathbf{U}}^{\dagger}(t + \Delta t, t) = \widehat{\mathbf{U}}^{-1}(t + \Delta t, t) \\ &\Rightarrow \langle \Psi(t)|\Psi(t)\rangle = \langle \Psi(t + \Delta t)|\Psi(t + \Delta t)\rangle \quad \forall\, t, \Delta t\ . \end{aligned} \tag{34}$$

Arbitrary times can therefore be reached by successive application of (31). The norm of the wave function is conserved for all times. For many practical problems the exponential in (31) can not be evaluated exactly but there exist many propagation schemes that provide different approximations (see [132] for a comprehensive review of different time-stepping techniques). In our approach, we use the *Short Iterative Lanczos* (SIL) propagation scheme, which will be briefly outlined below.

3.1 *Lanczos Propagation*

The Lanczos algorithm relies on Krylov subspace techniques that were originally introduced to calculate eigenvalues and eigenvectors of (large) matrices [133]. In the form presented here, it is only applicable for Hermitian matrices. The procedure works as follows:

A Krylov subspace of order $N+1$ is generated by the repeated action of $\widehat{\mathbf{H}}$ on an initial state $|\Psi_0\rangle$ (assumed to be normalized)

$$K_{N+1} = \{|\Psi_0\rangle, |\Psi_1\rangle, |\Psi_2\rangle, \ldots, |\Psi_N\rangle\} \tag{35}$$

$$|\Psi_k\rangle = \widehat{\mathbf{H}}^k |\Psi_0\rangle \ . \tag{36}$$

Orthonormalizing the basis vectors in the subspace by the Gram-Schmidt procedure produces a new basis,

$$\Lambda_{N+1} = \{|\lambda_0\rangle, |\lambda_1\rangle, |\lambda_2\rangle, \ldots, |\lambda_N\rangle\} \ . \tag{37}$$

The most time consuming step in the process is the application of $\widehat{\mathbf{H}}$ to a previously computed Lanczos vector. Given the sparse matrix representation inherent in the FEDVR, it is possible to reduce this to a set of small and structured matrix-vector multiplies using the matrices of the one-dimensional FEDVR blocks. These are individually small, dense systems whose size depends on the number of FEDVR functions used in that block. Thus the scaling of the matrix-vector multiply is significantly reduced from the more general case. The Hamiltonian $\widehat{\mathbf{H}}$ is then approximated as a $(N+1)\times(N+1)$ matrix $\widehat{\mathbf{H}}^{(\Lambda)}$ in the Λ_{N+1} basis. N is chosen much smaller than the dimension of the matrix representation of $\widehat{\mathbf{H}}$ (which can be up to 10^9), with typical values of $12-15$ in our case. Direct diagonalization of this small matrix can be efficiently performed. In the limit $N\to\infty$, the eigenvalues and eigenvectors of the transformed Hamiltonian converge to those of the full Hamiltonian, with the extreme (i.e., largest and smallest) eigenvalues converging first.

The Lanczos algorithm is very effective because in practice it is not necessary to explicitly build up the Krylov space and perform the full orthonormalization to all previous vectors, since the matrix $\widehat{\mathbf{H}}^{(\Lambda)}$ is tridiagonal and its elements can be obtained from a three-term recursion relation. This construction proceeds analogously to the construction of orthogonal polynomials, with $\widehat{\mathbf{H}}$ replacing the coordinate operator.

We thus get a *three-term recurrence relation*

$$|\lambda_0\rangle = |\Psi_0\rangle \tag{38}$$

$$\beta_0|\lambda_1\rangle = \widehat{\mathbf{H}}|\lambda_0\rangle - \alpha_0|\lambda_0\rangle \equiv |q_0\rangle \tag{39}$$

$$\beta_j|\lambda_{j+1}\rangle = \widehat{\mathbf{H}}|\lambda_j\rangle - \alpha_j|\lambda_j\rangle - \beta_{j-1}|\lambda_{j-1}\rangle \equiv |q_j\rangle \tag{40}$$

where $|\Psi_0\rangle$ is assumed to be normalized and

$$\alpha_j = \langle\lambda_j|\widehat{\mathbf{H}}|\lambda_j\rangle \tag{41}$$

$$\beta_j = \sqrt{\langle q_j|q_j\rangle}\,, \tag{42}$$

where both α_j and β_j are real. The Hamilton operator in the subspace Λ_{N+1} is thus real and tridiagonal and is given by

$$\widehat{\mathbf{H}}^{(\Lambda)}_{ij} = \langle\lambda_i|\widehat{\mathbf{H}}|\lambda_j\rangle \hat{=} \begin{pmatrix} \alpha_0 & \beta_0 & 0 & \cdots & 0 \\ \beta_0 & \ddots & \ddots & \ddots & \vdots \\ 0 & \ddots & \ddots & \ddots & 0 \\ \vdots & \ddots & \ddots & \ddots & \beta_{N-1} \\ 0 & \cdots & 0 & \beta_{N-1} & \alpha_N \end{pmatrix}. \tag{43}$$

To perform time propagation, we replace the Hamiltonian in the time evolution operator by its approximation in the Krylov subspace of $|\Psi(t)\rangle$ ($\equiv |\Psi_0\rangle$),

$$\widehat{\mathbf{U}}^{(\Lambda)} = \exp(-\mathrm{i}\widehat{\mathbf{H}}^{(\Lambda)}\Delta t)\,. \tag{44}$$

Consequently, $\widehat{\mathbf{U}}^{(\Lambda)}$ is restricted to the same Krylov subspace, where the exponential can be evaluated by direct diagonalization

$$\widehat{\mathbf{U}}^{(\Lambda)} = \sum_l |Z_l\rangle \exp\bigl(-\mathrm{i}h_l^{(\Lambda)}\Delta t\bigr)\langle Z_l|\,. \tag{45}$$

Here, $|Z_i\rangle$ denotes the eigenvector of $\widehat{\mathbf{H}}^{(\Lambda)}$ with the eigenvalue $h_j^{(\Lambda)}$.

The approximation for the propagated wave function then reads

$$|\Psi(t+\Delta t)\rangle = \widehat{\mathbf{U}}^{(\Lambda)}|\Psi(t)\rangle = \widehat{\mathbf{U}}^{(\Lambda)}|\Psi_0\rangle = \sum_{k=0}^{N} a_k|\lambda_k\rangle \tag{46}$$

with

$$a_k = \langle\lambda_k|\widehat{\mathbf{U}}^{(\Lambda)}|\lambda_0\rangle = \sum_l \langle\lambda_k|Z_l\rangle \exp\bigl(-\mathrm{i}h_l^{(\Lambda)}\Delta t\bigr)\langle Z_l|\lambda_0\rangle\,. \tag{47}$$

Since the $|\lambda_k\rangle$ are linear combinations of the $|\Psi_k\rangle$ which, in turn, are given by $|\Psi_k\rangle = \widehat{\mathbf{H}}^k|\Psi_0\rangle$, (46) is effectively a Nth-order polynomial expansion of the exponential in (31). Moreover, the Lanczos procedure generates a set of orthogonal

polynomials and for a finite Λ-dimensional operator (such as a Hamiltonian in a DVR representation) the approximation gets *exact* for $N \to \Lambda - 1$ [132]. In contrast to a standard Nth-order Taylor or Chebyshev expansion the coefficients a_k are optimized to give the best approximation for a given $|\Psi_0\rangle$ and in addition unitarity is conserved.

The Lanczos procedure can also be adapted for non-Hermitian operators using a biorthogonal basis. For complex symmetric operators, it can be more simply implemented, by performing the dot products without complex conjugation of the vectors. This also leads to a tridiagonal matrix. Another approach (known as the Arnoldi–Lanczos procedure [134]), transforms the original matrix to an upper Hessenberg matrix, which has zero entries below the first subdiagonal, in (43). This requires that the vectors have to be explicitly orthogonalized to all previous Krylov vectors, and entails considerably more numerical work. All of the above methods can be used to include complex absorbing potentials in the propagation scheme, as the Hamiltonian is then complex symmetric instead of Hermitian.

3.1.1 Split Operator Propagation

In some of the work described later in this article, we have employed split-operator techniques to propagate the time-dependent Schrödinger equation. These rely on approximating the exponential of the sum of two noncommuting operators $\widehat{\mathbf{A}}$ and $\widehat{\mathbf{B}}$ by a product of exponentials of the operators, i.e.,

$$\mathrm{e}^{(\widehat{\mathbf{A}}+\widehat{\mathbf{B}})t} = \mathrm{e}^{\widehat{\mathbf{A}}t/2}\mathrm{e}^{\widehat{\mathbf{B}}t}\mathrm{e}^{\widehat{\mathbf{A}}t/2} + O(t^3) \,, \tag{48}$$

where the third-order error term contains commutators of $\widehat{\mathbf{A}}$ and $\widehat{\mathbf{B}}$. Doing this for parts of the Hamiltonian in the time propagation operator and neglecting the third-order part gives a second-order approximation to propagating the Schrödinger equation. The propagation operator is then reduced to individual exponentials of each of the operators in the Hamiltonian.

A particular version of this is the Real-Space-Product (RSP) approach [135], which we use for propagating the Schrödinger equation for the H_2^+ molecular ion (Sect. 6). While the FEDVR kinetic energy operators are block-diagonal, the blocks overlap. Diagonalizing the whole kinetic energy operator thus destroys the sparsity of the matrix. We instead split it into two new operators such that each of the two gets alternating, nonoverlapping blocks. These new operators can be diagonalized by diagonalizing each separate FEDVR block, retaining the sparsity of the kinetic energy operator.

The split-operator method has also been used in the He code to prevent reflections at the grid boundary. By adding a *complex* absorbing potential of the form

$$A(r) = \mathrm{i}\alpha\theta(r - r_{\mathrm{cut}}) \ln\cos\left(\frac{r - r_{\mathrm{cut}}}{r_{\mathrm{max}} - r_{\mathrm{cut}}}\right) \tag{49}$$

to the Hamiltonian, it is possible to dampen the wave function to zero before it reaches the boundary. The potential and its first derivative are continuous functions, while the second derivative is discontinuous at $r_{\rm cut}$. The form of this particular potential is similar to a cosine-shaped "absorbing edge" masking function (as also employed in, e.g., [90]) and proved to be suitable for our purposes. Since adding this potential to the full Hamiltonian would make it non-Hermitian, we use the split-operator method,

$$\begin{aligned}\widehat{\mathbf{U}}(t, t+\Delta t) &= \exp(-\mathrm{i}\widehat{\mathbf{H}}(t)\Delta t - \mathrm{i}\hat{A}\Delta t) \\ &= \exp\left(-\mathrm{i}\hat{A}\frac{\Delta t}{2}\right)\exp(-\mathrm{i}\widehat{\mathbf{H}}(t)\Delta t)\exp\left(-i\,\hat{A}\frac{\Delta t}{2}\right) + O(\Delta t^3)\,. \end{aligned} \quad (50)$$

This has the considerable advantage of not requiring a non-Hermitian SIL procedure and is sufficiently accurate for our purposes. The effectiveness of such potentials always depends on the energy and the form of the incoming wave packet. In general, it is hard to completely avoid reflections. However, it is possible to suppress them below a certain level.[1]

3.1.2 Stability and Unitarity Considerations

The Krylov subspace approximation (45) for the time evolution operator is explicitly unitary. Therefore, the Lanczos algorithm is *unconditionally stable* and the propagation scheme is norm-conserving for Hermitian Hamiltonians. Consequently, the algorithm is also energy-conserving for time-independent operators.

Even though the propagation is explicitly unitary regardless of the properties of the discrete Hamiltonian, its spectrum still affects the propagation because large spectral ranges require small time steps or high orders to get accurate results. Thus, smaller grid spacings and more FEDVR basis functions make the temporal propagation computationally more costly.

4 Remarks on the Numerics and Computer Implementation

The number of angular momenta, number of radial points, extent of the radial grids, and propagation time that are needed to extract converged transition probabilities and/or cross sections depends sensitively on many factors. Care has to be taken to ensure that the basis is chosen such that, e.g., the Coulomb potential singularities at small distances and the highest energy electrons are represented well. Additionally, the question of whether one is interested in total or differential quantities determines the necessary basis sizes. Suffice it to say that by suitably arranging the density of finite elements and the order of the basis in each element, one is able to adequately converge the systems described in this article. The details of how to accomplish this

[1] See, e.g., [136, 137] for a detailed treatment of the problem.

are nontrivial, and will not be fully discussed in the current contribution. A further issue, which follows from the size of the basis set concerns the spectral range of the Hamiltonian. The highest eigenvalues of the Hamiltonian will fix the largest step size in time that can be used in the time propagation. While there are some ways that one can reduce the basis set by prediagonalization, the price that is paid is a loss of sparsity in the Hamiltonian matrix which is one of the most compelling reasons for using an FEDVR representation. Difficult choices have to be made but in general the computations can only be performed with substantial computational resources. The vector lengths may get as large as 10^9 for some cases and a parallel implementation using MPI on a large cluster with many cores is necessary. The calculations described here were performed using the US NSF TeraGrid systems at the National Institute for Computational Science at the University of Tennessee/Oak Ridge, the Texas Advanced Computer Center at the University of Texas/Austin, the Lobo and Coyote cluster at the Department of Energy Los Alamos National Laboratory, and the Vienna Scientific Cluster at the Vienna University of Technology. Without these computational instruments, much of the work described herein would have been impossible.

5 He

The first application of the foregoing method we discuss is the He atom. In this case, the nonrelativistic Hamiltonian is given by

$$\widehat{\mathbf{H}}(t) = \frac{\widehat{\mathbf{p}}_1^2}{2} + \frac{\widehat{\mathbf{p}}_2^2}{2} - \frac{Z}{r_1} - \frac{Z}{r_2} + \frac{1}{r_{12}} + \widehat{\mathbf{V}}_I(t) \,, \tag{51}$$

where the electron-field interaction operator in dipole approximation is

$$\widehat{\mathbf{V}}_I^L(t) = \boldsymbol{E}(t) \cdot (\widehat{\mathbf{r}}_1 + \widehat{\mathbf{r}}_2) \quad \text{or} \quad \widehat{\mathbf{V}}_I^V(t) = \boldsymbol{A}(t) \cdot (\widehat{\mathbf{p}}_1 + \widehat{\mathbf{p}}_2) \,, \tag{52}$$

with the superscript denoting the use of length (L) or velocity gauge (V), and $\boldsymbol{E}(t)$ and $\boldsymbol{A}(t)$ denoting, respectively, the electric field and the vector potential of the electromagnetic pulse. For the velocity gauge expression, the term $\boldsymbol{A}^2/2$ has been removed by adding a global time-dependent phase to the wave function. We proceed by expanding the six-dimensional wave function $\Psi(\mathbf{r}_1, \mathbf{r}_2)$ in coupled spherical harmonics,

$$\Psi(\mathbf{r}_1, \mathbf{r}_2, t) = \sum_{L,M}^{\infty} \sum_{l_1,l_2}^{\infty} \frac{R_{l_1,l_2}^{LM}(r_1, r_2, t)}{r_1 r_2} \mathcal{Y}_{l_1,l_2}^{LM}(\Omega_1, \Omega_2) \tag{53}$$

with

$$\mathcal{Y}_{l_1,l_2}^{LM}(\Omega_1, \Omega_2) = \sum_{m_1,m_2} \langle l_1 m_1 l_2 m_2 | LM \rangle \mathrm{Y}_{m_1}^{l_1}(\Omega_1) \mathrm{Y}_{m_2}^{l_2}(\Omega_2) \,. \tag{54}$$

Substituting (51) and (53) into (1), multiplying by $\mathcal{Y}_{l_1,l_2}^{LM}$, and integrating over all angles yields a system of coupled partial differential equations in (r_1, r_2, t), the time-dependent close coupling (TDCC) equations [138, 139]

$$\mathrm{i}\frac{\partial}{\partial t} R_{l_1',l_2'}^{LM}(r_1,r_2,t) = \sum_{L,M}^{\infty}\sum_{l_1,l_2}^{\infty} \langle l_1' l_2' L' M' | \widehat{\mathbf{H}} | l_1 l_2 L M \rangle R_{l_1,l_2}^{LM}(r_1,r_2,t)\,, \tag{55}$$

where in practice the sums have to be truncated at certain maximum angular momenta $(L_{\max}, l_{1,\max}, l_{2,\max})$. In what follows, we restrict ourselves to radiation polarized along the z-axis and initial states of the system with $M = 0$, where the projection of the angular momentum along the z-axis is zero. $\langle l_1', l_2' L' 0' | \widehat{\mathbf{H}} | l_1 l_2 L 0 \rangle$ is given by

$$\begin{aligned}
&\langle l_1' l_2' L' 0 | \widehat{\mathbf{H}} | l_1 l_2 L 0 \rangle \\
&= \delta_{LL'}\Bigg[\delta_{l_1 l_1'}\delta_{l_2 l_2'}\left(-\frac{1}{2}\frac{\partial^2}{\partial r_1^2} + \frac{l_1(l_1+1)}{2r_1^2} - \frac{Z}{r_1} - \frac{1}{2}\frac{\partial^2}{\partial r_2^2} + \frac{l_2(l_2+1)}{2r_2^2} - \frac{Z}{r_2}\right) \\
&\quad + W_{l_1,l_2,l_1',l_2'}^{L}(r_1,r_2) + V_{l_1,l_2,l_1',l_2'}^{LL'}(r_1,r_2,t)\Bigg]\,,
\end{aligned} \tag{56}$$

with the electron-electron interaction given by

$$\begin{aligned}
W_{l_1,l_2,l_1',l_2'}^{L}(r_1,r_2) &= \delta_{LL'}(-1)^L \sqrt{(2l_1+1)(2l_1'+1)(2l_2+1)(2l_2'+1)} \\
&\quad \times \sum_{\lambda=0}^{\infty}(-1)^{\lambda}\frac{r_<^{\lambda}}{r_>^{\lambda+1}} \begin{pmatrix} l_1 & \lambda & l_1' \\ 0 & 0 & 0 \end{pmatrix} \begin{pmatrix} l_2 & \lambda & l_2' \\ 0 & 0 & 0 \end{pmatrix} \begin{Bmatrix} L' & l_2' & l_1' \\ \lambda & l_1 & l_2 \end{Bmatrix}\,.
\end{aligned} \tag{57}$$

In the length gauge, the electron-field interaction is

$$\begin{aligned}
&V_{l_1,l_2,l_1',l_2'}^{LL'}(r_1,r_2,t) \\
&= E(t) c_{LL'} \begin{pmatrix} L & 1 & L' \\ 0 & 0 & 0 \end{pmatrix} \Bigg[r_1 (-1)^{l_2} c_{l_1 l_1'} \begin{pmatrix} l_1 & 1 & l_1' \\ 0 & 0 & 0 \end{pmatrix} \begin{Bmatrix} l_1 & l_2 & L \\ L' & 1 & l_1' \end{Bmatrix} \delta_{l_2' l_2} \\
&\quad + r_2 (-1)^{l_1} c_{l_2 l_2'} \begin{pmatrix} l_2 & 1 & l_2' \\ 0 & 0 & 0 \end{pmatrix} \begin{Bmatrix} l_2 & l_1 & L \\ L' & 1 & l_2' \end{Bmatrix} \delta_{l_1' l_1} \Bigg]\,,
\end{aligned} \tag{58}$$

while in the velocity gauge, it is

$$\begin{aligned}
&V_{l_1,l_2,l_1',l_2'}^{LL'}(r_1,r_2,t) \\
&= \mathrm{i}A(t)\sqrt{(2L+1)(2L'+1)} \begin{pmatrix} L & 1 & L' \\ 0 & 0 & 0 \end{pmatrix} \\
&\quad \times \Bigg[(-1)^{l_2} c_{l_1 l_1'} 1 \begin{pmatrix} l_1 & 1 & l_1' \\ 0 & 0 & 0 \end{pmatrix} \begin{Bmatrix} l_1 & l_2 & L \\ L' & 1 & l_1' \end{Bmatrix} \delta_{l_2' l_2} \left(\frac{\partial}{\partial r_1} - \frac{l_1'(l_1'+1) + l_1(l_1+1)}{2r_1} \right) \\
&\quad + (-1)^{l_1} c_{l_2 l_2'} \begin{pmatrix} l_2 & 1 & l_2' \\ 0 & 0 & 0 \end{pmatrix} \begin{Bmatrix} l_2 & l_1 & L \\ L' & 1 & l_2' \end{Bmatrix} \delta_{l_1' l_1} \left(\frac{\partial}{\partial r_2} - \frac{l_2'(l_2'+1) + l_2(l_2+1)}{2r_2} \right) \Bigg]\,,
\end{aligned} \tag{59}$$

where $c_{ij} = \overline{(2l_i+1)(2l_j+1)}$. The angular momentum selection rules restrict the coupling to being tridiagonal in L. The problem then reduces to a set of coupled two-dimensional, radial partial differential equations.

5.1 *Remarks on the Calculation of Two Electron Integrals*

The electron-electron interaction Hamiltonian $\widehat{\mathbf{W}}$ is represented in TDCC by

$$\langle k'|\widehat{\mathbf{W}}|k\rangle = \sum_{\lambda=0}^{\infty} \frac{r_<^\lambda}{r_>^{\lambda+1}} \widehat{\mathbf{W}}^{\text{ang}}_{k,k',\lambda} \,, \tag{60}$$

where $\widehat{\mathbf{W}}^{\text{ang}}_{k,k',\lambda}$ is the angular part of the electron-electron interaction operator, k and k' are the combined angular indices (L, l_1, l_2) and (L', l_1', l_2'), $r_<$ is $\min(r_1, r_2)$ and $r_>$ is $\max(r_1, r_2)$. The usual approximation for potentials in the FEDVR approach is to represent them as a diagonal matrix, with the entries just being the values of the potential at the grid points. However, this approach would entail a large error for the electron-electron interaction operator, as the radial part $r_<^\lambda / r_>^{\lambda+1}$ has a derivative discontinuity at $r_1 = r_2$, which can not simply be represented in the FEDVR basis. This can be fixed following the recipe of McCurdy et al. [140], a short summary of which is given in the following. The general idea behind this is to evaluate one of the radial integrals over FEDVR basis functions analytically, instead of using the Gauss–Lobatto quadrature associated with the grid. The radial parts of the interaction operator are given by the integrals

$$\begin{aligned}
&\left\langle f_{j_1} f_{j_2} \left| \frac{r_<^\lambda}{r_>^{\lambda+1}} \right| f_{j_1'} f_{j_2'} \right\rangle \\
&\quad = \int_0^{r_{\max}} \mathrm{d}r_1 \int_0^{r_{\max}} \mathrm{d}r_2 \, f_{j_1}(r_1) f_{j_1'}(r_1) \frac{r_<^\lambda}{r_>^{\lambda+1}} f_{j_2}(r_2) f_{j_2'}(r_2) \,,
\end{aligned} \tag{61}$$

where $f_j(r)$ is the jth FEDVR basis function. Instead of directly employing Gauss–Lobatto quadrature, we define the function

$$\begin{aligned}
y(r) &= r \int_0^{r_{\max}} \mathrm{d}r' \, \frac{r_<^\lambda}{r_>^{\lambda+1}} f_{j_2}(r') f_{j_2'}(r') \\
&= \int_0^r \mathrm{d}r' \, \frac{r'^\lambda}{r^\lambda} f_{j_2}(r') f_{j_2'}(r') + \int_r^{r_{\max}} \mathrm{d}r' \, \frac{r^{\lambda+1}}{r'^{\lambda+1}} f_{j_2}(r') f_{j_2'}(r') \,,
\end{aligned} \tag{62}$$

which satisfies the radial Poisson equation,

$$\left(\frac{\mathrm{d}^2}{\mathrm{d}r^2} - \frac{\lambda(\lambda+1)}{r^2} \right) y(r) = -\frac{2\lambda+1}{r} f_{j_2}(r) f_{j_2'}(r) \tag{63}$$

with the boundary conditions $y(0) = 0$ and $y(r_{\max}) = r_{j_2}^{\lambda}/r_{\max}^{\lambda}\delta_{j_2,j_2'}$. Expanding $y(r)$ in the basis of FEDVR functions, inserting into (63), solving the resulting matrix equation, and finally adding a solution of the homogeneous radial Poisson equation to satisfy the boundary conditions leads to

$$y(r) = (2\lambda + 1)\sum_{i=1}^{N}[T^{\lambda}]^{-1}_{i,j_2}\frac{f_i(r)}{r_{j_2}\sqrt{w_{j_2}}}\delta_{j_2,j_2'} + \frac{r_{j_2}^{\lambda}r^{\lambda+1}}{r_{\max}^{2\lambda+1}}\delta_{j_2,j_2'}\,, \tag{64}$$

where

$$T^{\lambda}_{i,j} = \left\langle f_i \middle| -\frac{\mathrm{d}}{\mathrm{d}r^2} + \frac{\lambda(\lambda+1)}{r^2}\middle| f_j \right\rangle \tag{65}$$

is twice the single-electron kinetic energy operator for angular momentum λ in the FEDVR basis, $[T^{\lambda}]^{-1}_{i,j}$ is the element i, j of its inverse, and w_j is the Gauss–Lobatto integration weight associated with grid point r_j. Inserting this expression for $y(r)$ back into the original (61) and performing the integral using the Gauss–Lobatto quadrature gives the final result

$$\begin{aligned}&\left\langle f_{j_1} f_{j_2}\middle|\frac{r_<^{\lambda}}{r_>^{\lambda+1}}\middle| f_{j_1'} f_{j_2'}\right\rangle \\ &\quad = \delta_{j_1,j_1'}\delta_{j_2,j_2'}\left(\frac{2\lambda+1}{r_{j_1}r_{j_2}\sqrt{w_{j_1}w_{j_2}}}[T^{\lambda}]^{-1}_{j_1,j_2} + \frac{r_{j_1}^{\lambda}r_{j_2}^{\lambda}}{r_{\max}^{2\lambda+1}}\right)\,,\end{aligned} \tag{66}$$

which remarkably is still diagonal in the FEDVR grid indices j_1, j_2. The inverse matrices only have to be calculated once at the start of the program, which does not incur a large computational overhead. The improved precision of this expression for the electron-electron interaction is considerable. As an example, the error in the ground-state energy (i.e., the deviation from the "real" ground state of the nonrelativistic Hamiltonian) is only 5.3×10^{-5} a.u. using this improved expression, while the error is 1.2×10^{-2} a.u. when using the "naive" expression for the interaction operator. This example was calculated using typical parameters for our simulations (FEDVR elements of order 11 with 4 a.u. extension, $l_{1,\max} = l_{2,\max} = 9$).

5.2 *Observables*

We exploit the fact that our time-dependent approach allows propagation of the wave packet for long times after the conclusion of the pulse. Once the distance between the two electrons has reached a large enough value, we can neglect the electron-electron interaction term, $\widehat{\mathbf{H}}_{12} = \left|\widehat{\mathbf{r}}_1 - \widehat{\mathbf{r}}_2\right|^{-1}$, which becomes insignificant for asymptotic distances. Consequently, we approximate the continuum by the exact solution of the (separable) stationary Schrödinger equation with the Hamiltonian without electron-electron interaction,

$$\widehat{\mathbf{H}}_0 = \frac{\widehat{\mathbf{p}}_1^2}{2} + \frac{\widehat{\mathbf{p}}_2^2}{2} - \frac{Z}{r_1} - \frac{Z}{r_2} \,. \tag{67}$$

If both electrons are far away from the nucleus and/or have high energies, it would also be possible to neglect the electron-nucleus interaction when constructing final states for double ionization. However, as in almost all cases there is single as well as double ionization, we retain the electron-nucleus interaction term. This also ensures that the approximate single-continuum and double-continuum eigenstates are orthogonal to each other.

The separable Hamiltonian (67) is just the sum of two independent one-particle Hamiltonians. Before constructing the two-electron product states for the single and double continuum, we summarize some of the properties of the (analytic) eigenfunctions of the single-particle Hamiltonian of a hydrogen-like atom, with

$$\widehat{\mathbf{H}}_1 = \frac{\widehat{\mathbf{p}}^2}{2} - \frac{Z_{\text{eff}}}{r} \,. \tag{68}$$

As (68) is spherically symmetric, its eigenstates can be separated into a radial and an angular part,

$$\Phi_{k,l,m}(\mathbf{r}) = \frac{\phi_{k,l}(r)}{r} \mathrm{Y}_m^l(\Omega) \,, \tag{69}$$

where the angular part is described by the spherical harmonics $\mathrm{Y}_m^l(\Omega)$. For the *bound states*, the radial part of the regular eigenfunction is given by [141]

$$\phi_{n,l}(r) = \frac{\sqrt{Z_{\text{eff}}}}{n} \sqrt{\frac{(n-l-1)!}{(n+l)!}} \left(\frac{2Z_{\text{eff}} r}{n}\right)^{l+1} L_{n-l-1}^{2l+1}\left(\frac{2Z_{\text{eff}} r}{n}\right) \exp\left(-\frac{Z_{\text{eff}} r}{n}\right) \tag{70}$$

where L stands for the generalized Laguerre polynomial and $n \geq 1$ is the main quantum number. The eigenenergies of the bound states are given by

$$E_n = -\frac{Z_{\text{eff}}^2}{2n^2} \,. \tag{71}$$

The regular solution for the *unbound states* is given by the regular radial *Coulomb function* $F_l(\eta, kr)$ [141]

$$\begin{aligned} \phi_{k,l}(r) &= \sqrt{\frac{2}{\pi}} F_l(\eta, kr) \,, \\ F_l(\eta, kr) &= 2^l \mathrm{e}^{-\pi\eta/2} \frac{|\Gamma(l+1+\mathrm{i}\eta)|}{(2l+1)!} \mathrm{e}^{-\mathrm{i}kr} (kr)^{l+1} F(l+1-\mathrm{i}\eta, 2l+2; 2\mathrm{i}kr) \end{aligned} \tag{72}$$

with the confluent hypergeometric series F

$$F(a,b;z) = \sum_{n=0}^{\infty} \frac{\Gamma(a+n)}{\Gamma(a)} \frac{\Gamma(b)}{\Gamma(b+n)} \frac{z^n}{n!} \,, \tag{73}$$

which in the limit $r \to \infty$ behave as

$$F_l(\eta, kr) \to \sin\left(kr - \eta \ln 2kr - \frac{l\pi}{2} + \sigma_l\right) , \tag{74}$$

with the *Coulomb phase* $\sigma_l = \arg[\Gamma(l+1+\mathrm{i}\eta)]$. In (72) we introduced the Coulomb parameter η, which determines the strength of the Coulomb term in (68),

$$\eta = -\frac{Z_{\text{eff}}}{k} . \tag{75}$$

Inserting the radial part (72) back into (69) yields the *spherical Coulomb waves* $\Phi_{k,l,m}(\mathbf{r})$, which are eigenfunctions of (68), orthonormalized in momentum k, total angular momentum $\mathbf{L}^2$, and the z-component L_z of angular momentum,

$$\langle \Phi_{k,l,m} | \Phi_{k',l',m'} \rangle = \delta(k - k')\delta_{ll'}\delta_{mm'} . \tag{76}$$

Since k is a continuous variable, the wave functions are normalized to the Dirac delta function (or distribution), while the discrete quantum numbers l, m are orthonormalized to a Kronecker delta. Instead of normalizing in momentum space, we can also use *energy-normalized* radial Coulomb functions. Due to

$$\delta(k - k') = \frac{\mathrm{d}E}{\mathrm{d}k}\delta(E - E') , \quad k = \sqrt{2E} , \tag{77}$$

they are related to the momentum-normalized functions (72) according to

$$\phi_{E,l}(r) = \frac{\phi_{k,l}(r)}{\sqrt{k}} . \tag{78}$$

If we are not interested in the angular momentum quantum numbers, but want to specify a 3-vector $\mathbf{k} \equiv (k, \Omega_k)$ for the momentum, we can use the expansion

$$\psi_{\mathbf{k}}(\mathbf{r}) = \sum_{l=0}^{\infty} \sum_{m=-l}^{l} i^l \mathrm{e}^{-\mathrm{i}\sigma_l} \mathrm{Y}_m^{*(l)}(\Omega_k) \Phi_{k,l}(\mathbf{r}) . \tag{79}$$

These functions are the solutions of the Coulomb problem satisfying incoming scattering boundary conditions that converge asymptotically to eigenstates of linear momentum $\mathbf{k}$. *Incoming* boundary conditions are the appropriate basis states for extracting ionization probabilities [142–144].

Using these *one-electron* eigenfunctions, we construct the *double continuum* wave functions as symmetrized product states of two unscreened Coulomb waves (79) with effective charge $Z_{\text{eff}} = 2$, where the symmetrization is necessary to account for the indistinguishability of the two electrons. For $\mathbf{k}_1 \neq \mathbf{k}_2$, these states (in singlet spin symmetry) are given by

$$\Psi^{\text{DC}}_{\mathbf{k}_1,\mathbf{k}_2}(\mathbf{r}_1, \mathbf{r}_2) = \frac{1}{\sqrt{2}}[\psi_{\mathbf{k}_1}(\mathbf{r}_1)\psi_{\mathbf{k}_2}(\mathbf{r}_2) + \psi_{\mathbf{k}_1}(\mathbf{r}_2)\psi_{\mathbf{k}_2}(\mathbf{r}_1)] . \tag{80}$$

The use of a product final state amounts to neglecting the effect of electron-electron interaction, which is a good approximation only in the asymptotic regime ($r_{12} \to \infty$).

It should be noted that in our approach of solving the TDSE, we only need the double-continuum wave functions in the asymptotic region for extraction of the final momentum distributions. The correlation is thus included in the calculation at each step, the only approximation is the identification of the momenta $\mathbf{k}_1, \mathbf{k}_2$ in the product state with the asymptotic momenta of the two electrons. In other approaches, such as time-independent perturbation theory, it is much more crucial to use an accurate representation of the continuum. This can be achieved in a number of ways, e.g., by using so-called 3C wave functions [145, 146] which consist of a product of three two-body Coulomb functions. Another approach is to use the techniques of exterior complex scaling (ECS) in combination with formal scattering theory, which can be used to extract the double ionization amplitudes by a surface integral at the edge of the box, where the product of Coulomb waves is again a good approximation if the box is large enough [140, 147, 148]. A third approach to get the double ionization wave function is to use the J-matrix method to generate fully correlated multichannel scattering wave functions for the single continuum and then obtain the double ionization wave packet by subtracting the bound and singly ionized parts from the total wave function [80].

Inserting the partial-wave expansion (79) into (80) and switching to coupled spherical harmonics yields the double-continuum wave function in coordinate space,

$$\begin{aligned}\Psi^{\mathrm{DC}}_{\mathbf{k}_1,\mathbf{k}_2}(\mathbf{r}_1,\mathbf{r}_2) = \sum_{L,M}^{\infty}\sum_{l_1,l_2}^{\infty} i^{l_1+l_2}\mathrm{e}^{-\mathrm{i}(\sigma_{l_1}+\sigma_{l_2})}[\mathcal{Y}^{LM}_{l_1,l_2}(\Omega_{k,1},\Omega_{k,2})]^* \frac{1}{\sqrt{2}}\frac{1}{r_1 r_2} \\ \times [\phi_{k_1,l_1}(r_1)\phi_{k_2,l_2}(r_2)\mathcal{Y}^{LM}_{l_1,l_2}(\Omega_{r,1},\Omega_{r,2}) \\ + \phi_{k_1,l_1}(r_2)\phi_{k_2,l_2}(r_1)\mathcal{Y}^{LM}_{l_1,l_2}(\Omega_{r,2},\Omega_{r,1})] \,. \end{aligned} \tag{81}$$

In analogy, we construct the *single continuum* as a symmetrized product state of a *bound state* $\Phi_{n,l,m}(\mathbf{r})$ of the He^+ ion and a Coulomb wave $\psi_{\mathbf{k}}(\mathbf{r})$ with effective charge $Z_{\mathrm{eff}} = 1$,

$$\Psi^{\mathrm{SC}}_{n,l,m,\mathbf{k}}(\mathbf{r}_1,\mathbf{r}_2) = \frac{1}{\sqrt{2}}[\Phi_{n,l,m}(\mathbf{r}_1)\psi_{\mathbf{k}}(\mathbf{r}_2) + \Phi_{n,l,m}(\mathbf{r}_2)\psi_{\mathbf{k}}(\mathbf{r}_1)] \,. \tag{82}$$

Inserting the partial-wave expansion for the Coulomb wave and the coordinate representation of $\Phi_{n,l,m}(\mathbf{r})$ yields the single-continuum wave function in coordinate space. The bound state is not expanded into a function of a wave vector (as in (79) for the continuum wave) leaving a Clebsch–Gordan coefficient from switching to the coupled angular momentum representation,

$$\Psi^{\mathrm{SC}}_{n,l,m,\mathbf{k}}(\mathbf{r}_1,\mathbf{r}_2)$$

$$= \sum_{L,M}^{\infty} \sum_{l_k=0}^{\infty} \sum_{m_k=-l_k}^{l_k} i^{l_k} \mathrm{e}^{-\mathrm{i}\sigma_{l_k}} [\mathrm{Y}_{m_k}^{l_k}(\Omega_k)]^* \langle l m l_k m_k | l l_k L M \rangle \frac{1}{\sqrt{2}} \frac{1}{r_1 r_2}$$
$$\times [\phi_{n,l,}(r_1)\phi_{k,l_k}(r_2)\mathcal{Y}_{l_1,l_2}^{LM}(\Omega_{r,1}, \Omega_{r,2})$$
$$+ \phi_{n,l}(r_2)\phi_{k,l_k}(r_1)\mathcal{Y}_{l_1,l_2}^{LM}(\Omega_{r,2}, \Omega_{r,1})] \,. \tag{83}$$

5.3 *Ionization Probability Distributions*

5.3.1 Fully Differential Probability Distributions

By projecting the single- and double-continuum functions constructed in the previous section onto the fully correlated final state wave function, we obtain momentum probability distributions. The electron momentum distribution for *double ionization* is given by

$$P^{\mathrm{DI}}(\mathbf{k}_1, \mathbf{k}_2) = P^{\mathrm{DI}}(k_1, k_2, \Omega_{k,1}, \Omega_{k,2}) = \left| \langle \Psi_{\mathbf{k}_1,\mathbf{k}_2}^{\mathrm{DC}} | \Psi \rangle \right|^2 \,. \tag{84}$$

Using the expression (81) for the double continuum and (53) for the calculated wave function (for which $M = 0$ because of cylindrical symmetry) yields

$$P^{\mathrm{DI}}(\mathbf{k}_1, \mathbf{k}_2)$$
$$= \frac{1}{2} \Bigg| \sum_{L}^{\infty} \sum_{l_1,l_2}^{\infty} \mathrm{i}^{-l_1-l_2} \mathrm{e}^{\mathrm{i}(\sigma_{l_1}+\sigma_{l_2})} \mathcal{Y}_{l_1,l_2}^{L0}(\Omega_{k,1}, \Omega_{k,2})$$
$$\times \int_0^{\infty} \int_0^{\infty} \mathrm{d}r_1 \, \mathrm{d}r_2 \, R_{l_1,l_2}^{L}(r_1, r_2)[\phi_{k_1,l_1}(r_1)\phi_{k_2,l_2}(r_2)$$
$$+ \phi_{k_1,l_1}(r_2)\phi_{k_2,l_2}(r_1)] \Bigg|^2 \,, \tag{85}$$

where we used the orthonormality relation

$$\langle \mathcal{Y}_{l_1,l_2}^{LM} | \mathcal{Y}_{l_1',l_2'}^{L'M'} \rangle = \delta_{LL'} \delta_{l_1 l_1'} \delta_{l_2 l_2'} \delta_{MM'} \tag{86}$$

for the evaluation of the angular part of the integral in position space, and the fact that the Coulomb wave functions can be chosen real. Furthermore, we can use the exchange symmetry for the wave function $|\psi\rangle$

$$R_{l_2,l_1}^{L}(r_2, r_1) = (-1)^{(l_1+l_2-L)} R_{l_1,l_2}^{L}(r_1, r_2) \tag{87}$$

and obtain for the double ionization probability distribution

$$P^{\mathrm{DI}}(\mathbf{k}_1,\mathbf{k}_2)=\left|\sum_{L}^{\infty}\sum_{l_1,l_2}^{\infty}\mathrm{i}^{-l_1-l_2}\mathrm{e}^{\mathrm{i}(\sigma_{l_1}+\sigma_{l_2})}\mathcal{Y}^{L0}_{l_1,l_2}(\Omega_{k,1},\Omega_{k,2})P^{L}_{l_1,l_2}(k_1,k_2)\right|^2 \quad (88)$$

with

$$P^{L}_{l_1,l_2}(k_1,k_2)=\sqrt{2}\int_0^\infty\int_0^\infty \mathrm{d}r_1\,\mathrm{d}r_2\,R^{L}_{l_1,l_2}(r_1,r_2)\phi_{k_1,l_1}(r_1)\phi_{k_2,l_2}(r_2)\,. \quad (89)$$

For the six-dimensional *single ionization* probability distribution we find a similar expression,

$$P^{\mathrm{SI}}(n,l,m,\mathbf{k})=\left|\sum_{L}^{\infty}\sum_{l_k=0}^{\infty}\sum_{m_k=-l_k}^{l_k}(-\mathrm{i})^{l_k}\mathrm{e}^{\mathrm{i}\sigma_{l_k}}\,\mathrm{Y}^{l_k}_{m_k}(\Omega_k)\times\langle l m l_k m_k|l\,l_k L0\rangle\,P^{L}_{l_1,l_2}(n,k)\right|^2 \quad (90)$$

with

$$P^{L}_{l_1,l_2}(n,k)=\sqrt{2}\int_0^\infty\int_0^\infty \mathrm{d}r_1\,\mathrm{d}r_2\,R^{L}_{l_1,l_2}(r_1,r_2)\phi_{n,l}(r_1)\phi_{k,l_k}(r_2)\,. \quad (91)$$

Instead of using distributions differential in *momentum*, it is equally possible to use *energy* differential distributions, which can be described by the the same expressions, except for the use of energy-normalized Coulomb functions $\phi_{E,l}$ (78) instead of $\phi_{k,l}$ in (89) and (91).

The fully differential probability distributions (88) and (90) contain all the information about the final state momenta of the electrons. Often, it is more interesting to look at lower-dimensional distributions, obtained either by integrating out some variables of the full distribution or by choosing specific *cuts* in the six-dimensional space.

5.3.2 Energy Probability Distributions

Integrating out the angles Ω_1,Ω_2 in (88) gives the joint energy probability distribution for the two (ejected) electrons in a double ionization process

$$P^{\mathrm{DI}}(E_1,E_2)=\sum_{L}^{\infty}\sum_{l_1,l_2}^{\infty}\left|P^{L}_{l_1,l_2}(E_1,E_2)\right|^2\,. \quad (92)$$

Further integrating over E_1 or E_2 gives the single-electron energy probability distribution for double ionization,

$$P^{\mathrm{DI}}(E)=\int_0^\infty P^{\mathrm{DI}}(E_1,E_2)\mathrm{d}E_1=\int_0^\infty P^{\mathrm{DI}}(E_1,E_2)\,\mathrm{d}E_2\,, \quad (93)$$

i.e., the probability for one detected electron to have the energy E.

5.3.3 Angular Probability Distributions

More detailed information about a double ionization event is provided by angular differential distributions. The joint angular distribution is obtained by integrating over the energies of both electrons,

$$P^{\mathrm{DI}}(\Omega_{k,1}, \Omega_{k,2}) = \int_0^\infty \int_0^\infty P^{\mathrm{DI}}(E_1, E_2, \Omega_{k,1}, \Omega_{k,2})\, \mathrm{d}E_1\, \mathrm{d}E_2 \ . \tag{94}$$

This gives the distribution in angles, regardless of the energies of the electrons. By dropping the integration over one of the energies, one obtains the angle-energy probability distribution, which can reveal correlations between the angular and energy degrees of freedom.

An additional observable of interest is the one-electron angular distribution, which can be characterized by the anisotropy parameters β_j, as shown in the following. The one-electron probability distribution $P^{\mathrm{DI}}(E_1, \Omega_{k,1})$ for one electron with respect to the laser polarization axis is given by integrating (88) over E_2 and $\Omega_{k,2}$. Because of the total cylindrical symmetry in the system, the resulting one-electron probability distribution is independent of the azimuthal angle φ_1. In the following, we therefore integrate over φ_1, and consequently, $P^{\mathrm{DI}}(E_1, \theta_1) = 2\pi P^{\mathrm{DI}}(E_1, \Omega_{k,1})$, and

$$P^{\mathrm{DI}}(E_1, \theta_1) = \iiint P^{\mathrm{DI}}(E_1, E_2, \Omega_{k,1}, \Omega_{k,2})\, \mathrm{d}E_2\, \mathrm{d}\Omega_{k,2}\, \mathrm{d}\varphi_1 \ . \tag{95}$$

Due to the indistinguishability of the two electrons it follows that

$$P^{\mathrm{DI}}(E_1, \theta_1) = P^{\mathrm{DI}}(E_2, \theta_2) = P^{\mathrm{DI}}(E, \theta) \ . \tag{96}$$

This expression can be characterized by the angular anisotropy parameters[2] β_j (cf.,e.g., [92]) that are obtained by projecting $P^{\mathrm{DI}}(E, \theta)$ on Legendre polynomials $P_l(\cos\theta)$,

$$P^{\mathrm{DI}}(E, \theta) = P^{\mathrm{DI}}(E) \sum_{j=0}^{\infty} \beta_j(E) P_j(\cos\theta) \ , \tag{97}$$

where the energy differential ionization probability $P^{\mathrm{DI}}(E)$ has been factored out of the sum so that $\beta_0(E) = 1$, as the integral over the Legendre polynomials is zero for $j \neq 0$. For ionization by a specified number of photons (i.e., if there is no interference between processes with different photon numbers), the parity of the wave function is well-defined, and the coefficients of Legendre polynomials with odd j vanish. This can be seen in (101) from the 3j-symbol containing j, L and L', with all magnetic quantum numbers equal to zero (the *parity 3j-symbol*), which is zero for odd $j + L + L'$. As L and L' are either both odd or both even ($L = 1$ for

[2] Often the labeling $\beta = \beta_2$ and $\gamma = \beta_4$ is used instead [79].

one-photon transitions, $L = 0, 2$ for two-photon transitions, $L = 1, 3, 5$ for three-photon transitions, ...), $L + L'$ is always even. Therefore, j also has to be even. In addition, because of the triangle inequality in the parity 3j-symbol, the highest j occurring in an n-photon transition from a state with $L = 0$ is $j = 2n$.

The anisotropy parameters can be expressed by inserting the electron momentum distribution for double ionization (88) into (95) and analytically performing the integration

$$\begin{aligned} P^{\mathrm{DI}}(E_1, \theta_1) &= \int_0^\infty \int_{\Omega_2} \int_0^{2\pi} P^{\mathrm{DI}}(E_1, E_2, \Omega_1, \Omega_2)\, \mathrm{d}E_2\, \mathrm{d}\Omega_2\, \mathrm{d}\varphi_1 \\ &= \int_0^\infty \int_{\Omega_2} \int_0^{2\pi} \Bigg| \sum_L^\infty \sum_{l_1,l_2}^\infty \mathrm{i}^{-l_1-l_2} \mathrm{e}^{\mathrm{i}(\sigma_{l_1}+\sigma_{l_2})} \mathcal{Y}^{L0}_{l_1,l_2}(\Omega_1, \Omega_2) \\ &\quad \times P^L_{l_1,l_2}(E_1, E_2) \Bigg|^2 \mathrm{d}E_2\, \mathrm{d}\Omega_2\, \mathrm{d}\varphi_1 \,. \end{aligned} \tag{98}$$

For brevity we will use

$$D^L_{l_1,l_2}(E_1, E_2) = \mathrm{i}^{-l_1-l_2} \mathrm{e}^{\mathrm{i}(\sigma_{l_1}+\sigma_{l_2})} P^L_{l_1,l_2}(E_1, E_2) \tag{99}$$

in the following formulas. This corresponds to an expansion in our coupled basis representation in energy space, thus expressing the doubly ionized wave function $\Psi^{\mathrm{DI}}(E_1, E_2, \Omega_{k,1}, \Omega_{k,2})$ in coupled spherical harmonics,

$$\Psi^{\mathrm{DI}}(E_1, E_2, \Omega_{k,1}, \Omega_{k,2}) = \sum_L^\infty \sum_{l_1,l_2}^\infty D^L_{l_1,l_2}(E_1, E_2) \mathcal{Y}^{L0}_{l_1,l_2}(\Omega_{k,1}, \Omega_{k,2}) \,. \tag{100}$$

The integrals over the angles can be performed analytically. The final result for the angular probability distribution $P^{\mathrm{DI}}(E_1, \theta_1)$ is then

$$\begin{aligned} P^{\mathrm{DI}}(E_1, \theta_1) = \sum_j \sum_{\substack{L', l_1' \\ L, l_1, l_2}} & (-1)^{j-L-L'-l2} \sqrt{(2l_1+1)(2l_1'+1)(2L+1)(2L'+1)} \\ & \times (2j+1) \begin{pmatrix} l_1 & l_1' & j \\ 0 & 0 & 0 \end{pmatrix} \begin{pmatrix} j & L & L' \\ 0 & 0 & 0 \end{pmatrix} \begin{Bmatrix} j & l_1 & l_1' \\ l_2 & L' & L \end{Bmatrix} (D^{L'}_{l_1',l_2})^* D^L_{l_1,l_2} \\ & \times P_j(\cos\theta_1) \,. \end{aligned} \tag{101}$$

For $j = 2$ this formula coincides with the expression for β parameters presented by Kheifets et al. [92] and an analogous expression for β parameters of two-photon single ionization by Gribakin et al. [149].

5.3.4 Angular Distribution for Single Ionization

Similar to the one-electron angular distribution for double ionization expressed in terms of the anisotropy parameters, we define the analogous probability distribution for single ionization by summing over the states of the bound electron

$$P^{\mathrm{SI}}(E,\theta) = \sum_{n,l,m} \int P^{\mathrm{SI}}(n,l,m,E,\Omega_k)\,\mathrm{d}\varphi \;, \tag{102}$$

with $P^{\mathrm{SI}}(n,l,m,E,\Omega_k)$ defined in (90). The derivation is similar to the one for the double ionization angular distribution,

$$\begin{aligned}
&\psi^{\mathrm{SI}}(n,l,m,E,\Omega_k) \\
&= \sum_{L}^{\infty} \sum_{l_k=0}^{\infty} \sum_{m_k=-l_k}^{l_k} (-\mathrm{i})^{l_k}\, \mathrm{e}^{\mathrm{i}\sigma_{l_k}}\, \mathrm{Y}_{m_k}^{l_k}(\Omega_k) \begin{bmatrix} l & l_k & L \\ m & m_k & 0 \end{bmatrix} P_{l_1,l_2}^{L}(n,E) \;,
\end{aligned} \tag{103}$$

with $P_{l_1,l_2}^{L}(n,E)$ given in (91) and the square brackets denoting a Clebsch–Gordan coefficient. Instead of performing the integral over the continuum states of the second electron, we take the sum over the bound states

$$\int \mathrm{d}E_2\,\mathrm{d}\Omega_{k,2} \longrightarrow \sum_{n,l} \sum_{m=-l}^{l} \;. \tag{104}$$

This yields

$$P^{\mathrm{SI}}(E,\theta_k) = \sum_{j} \beta_j(E)\, P_j(\cos\theta_k) \;, \tag{105}$$

with

$$\begin{aligned}
\beta_j(k) = \sum_{n,l} \sum_{\substack{L',l'_k \\ L,l_k}} (-1)^{j-L-L'-l} &\sqrt{(2l_k+1)(2l'_k+1)(2L+1)(2L'+1)}(2j+1) \\
&\begin{pmatrix} l_k & l'_k & j \\ 0 & 0 & 0 \end{pmatrix} \begin{pmatrix} j & L & L' \\ 0 & 0 & 0 \end{pmatrix} \begin{Bmatrix} j & l_k & l'_k \\ l & L' & L \end{Bmatrix} \left((-\mathrm{i})^{l'_k}\, \mathrm{e}^{\mathrm{i}\sigma_{l'_k}}\, P_{l'_k,l}^{L'}(n,k)\right)^{*} \\
&\times \left((-\mathrm{i})^{l_k}\, \mathrm{e}^{\mathrm{i}\sigma_{l_k}}\, P_{l_k,l}^{L}(n,k)\right) \;.
\end{aligned} \tag{106}$$

The different bound states (n,l,m) are summed up incoherently in (106). For a fixed n,l,m, we get the probability distribution for the free electron associated with production of the He^{+} ion in different excited (shake-up) states (e.g., 1s, 2s, 2p, ...).

5.4 *Total Cross Sections*

Integrating (85) over all variables including E_1 and E_2 gives the total double ionization yield. Up to prefactors, it also gives an approximation for the total double ionization cross section for a suitably chosen pulse. The dependence on the primary photon energy is only implicit through the electromagnetic pulse entering the propagation. Within a time-dependent calculation, the resulting double ionization (DI) probability depends on the spectral distribution, i.e., the shape and duration of the laser pulse, while the fundamental quantity of interest, the DI cross section (DICS) at fixed frequency of the ionizing radiation does not. Extraction of the DICS therefore requires special care. For the case of one-photon ionization, it is straightforward to relate the energy-dependent yield to the cross section. From a single pulse, one can thus calculate the cross section for all energies contained within the pulse [80, 102]. This is not possible (without additional approximations, such as used in [106]) for two- or multiphoton ionization, since the relation between cross section and yield contains an integral over intermediate energies. For the evaluation of this integral, the intermediate states and energies would have to be explicitly available. This is not easily possible in the current approach without losing the key advantage of the time-dependent method of not having to construct intermediate or final states explicitly. The simplest alternative is to use a sufficiently long pulse with narrow spectral width and calculate the cross section from the total yield with the approximation that it is constant over the width of the pulse. For this approximation to be valid, the spectral width of the pulse must be smaller than the energy width over which the cross section significantly changes. We can check the convergence by varying the pulse length. Figures 4 and 5 illustrate this for both the joint two-electron energy distribution $P^{\mathrm{DI}}(E_1, E_2)$ (Fig. 4) and the integral (Fig. 5) along lines of constant total energy $E_1 + E_2$ in Fig. 4 for three different pulses, with durations of $T = 1\,\mathrm{fs}$ ($\sim$ 10 cycles), $T = 4\,\mathrm{fs}$ ($\sim$ 40 cycles), and $T = 9\,\mathrm{fs}$ ($\sim$ 90 cycles). While the 4 fs pulse is sufficient to resolve the cross section a few eV above the threshold, the shorter pulse (frequently employed, see [72, 76, 80, 86]) results in averaging over the threshold region. Close to the sequential threshold, the 9 fs pulse, or even longer ones, are necessary to resolve the detailed structure of the cross section.

Another requirement is that the pulse has to be weak enough such that lowest order perturbation theory is applicable and that ground-state depletion can be neglected. We therefore choose a peak intensity of $I_0 = 10^{12}\,\mathrm{W/cm^2}$. Variation between $10^{11}\,\mathrm{W/cm^2}$ and $10^{13}\,\mathrm{W/cm^2}$ results in deviations for the total cross section at 42 eV of less than 0.3%. For an intensity of $10^{13}\,\mathrm{W/cm^2}$, the two-photon yield is a factor of 10^4 higher than with $10^{11}\,\mathrm{W/cm^2}$.

Another test for applicability of perturbation theory is the linear scaling of the yield with the total duration T of the pulse, i.e., the transition rate must be proportional to $\Phi(t)^N$, where $\Phi(t) = I(t)/\omega$ is the photon flux and N is the minimum number of photons required for the process to take place. The double ionization yield is then given by

$$P^{\mathrm{DI}}_{\mathrm{nonseq}} = \int_{-\infty}^{\infty} \mathrm{d}t\, \sigma_N \Phi(t)^N \ , \tag{107}$$

where σ_N is the total generalized N-photon cross section for double ionization of He. Accordingly, the cross section is given by

$$\sigma_N \approx \left(\frac{\omega}{I_0}\right)^N \frac{1}{T_{\mathrm{eff},N}} \iiiint \mathrm{d}E_1\, \mathrm{d}E_2\, \mathrm{d}\Omega_1\, \mathrm{d}\Omega_2\, P^{\mathrm{DI}}(E_1, E_2, \Omega_1, \Omega_2) \ , \tag{108}$$

where the effective time $T_{\mathrm{eff},N}$ for an N-photon process is defined as

$$T_{\mathrm{eff},N} = \int_{-\infty}^{\infty} \mathrm{d}t \left(\frac{I(t)}{I_0}\right)^N \ . \tag{109}$$

For a $\sin^2$ pulse envelope and a two-photon process, $T_{\mathrm{eff},2}$ is found to be $35T/128$ [72, 80, 86]. (108) is valid for direct, i.e., nonsequential double ionization when no on-shell intermediate state is involved.

5.5 *Differential Cross Sections*

The triply differential cross section (TDCS) for emitting one electron with energy E_1 into the solid angle Ω_1, while the second one is emitted into Ω_2 follows from (108) as

$$\frac{\mathrm{d}\sigma_N}{\mathrm{d}E_1\, \mathrm{d}\Omega_1\, \mathrm{d}\Omega_2} = \left(\frac{\omega}{I_0}\right)^N \frac{1}{T_{\mathrm{eff},N}} \int \mathrm{d}E_2\, P^{\mathrm{DI}}(E_1, E_2, \Omega_1, \Omega_2) \ . \tag{110}$$

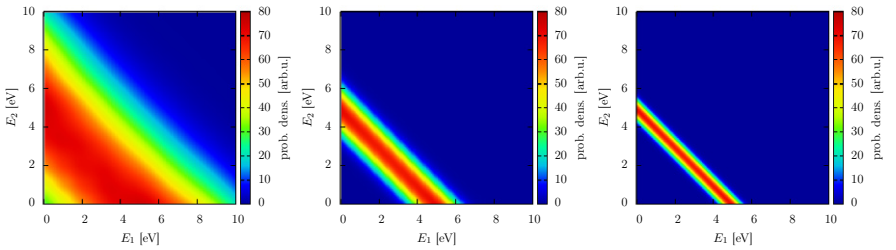

(a) 1 fs $\sin^2$ pulse (b) 4 fs $\sin^2$ pulse (c) 9 fs $\sin^2$ pulse

Fig. 4 Energy distribution after two-photon double ionization from three different laser pulses with a mean energy of $\langle\omega\rangle = 42\,\mathrm{eV}$. All three pulses have a $\sin^2$ envelope for the vector potential, with total durations (a) 1 fs ($\sim$ 10 cycles), (b) 4 fs ($\sim$ 40 cycles), (c) 9 fs ($\sim$ 90 cycles). The distributions are centered around the line $E_1 + E_2 = 2\langle\omega\rangle - I_1 - I_2 \approx 5\,\mathrm{eV}$. The width of the distribution directly shows the energy uncertainty due to Fourier broadening.

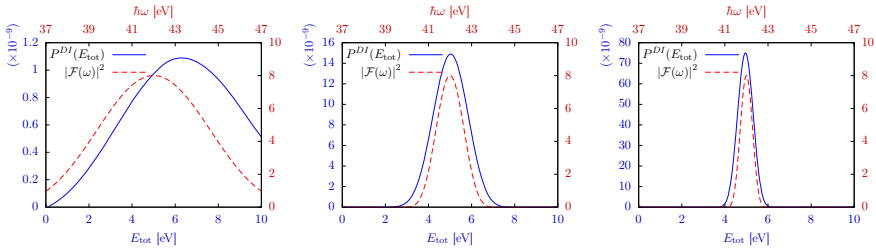

(a) 1 fs $\sin^2$ pulse (b) 4 fs $\sin^2$ pulse (c) 9 fs $\sin^2$ pulse

Fig. 5 Total energy distribution $P^{\mathrm{DI}}(E_{\mathrm{tot}})$ and Fourier spectra of 1 fs, 4 fs and 9 fs $\sin^2$ laser pulses. $P^{\mathrm{DI}}(E_{\mathrm{tot}})$ is the integral over lines with $E_{\mathrm{tot}} = E_1 + E_2$ from Fig. 4. The left and lower axes describe $P^{\mathrm{DI}}(E_{\mathrm{tot}})$, the right and upper axes describe $|\mathcal{F}(\omega)|^2$, the Fourier transform of $A(t)$. For the 4 fs and 9 fs pulses, the double ionization probability directly reflects the Fourier spectrum. For the shorter pulse the electron energy distribution is strongly influenced by the energy dependence of the cross section (cf. Fig. 6).

In the limit of an infinitely long laser pulse with well-defined energy (i.e., a delta-like spectrum), (110) becomes equivalent to

$$\left(\frac{\omega}{I_0}\right)^N \frac{1}{T_{\mathrm{eff},N}} \int \mathrm{d}E_2\, P^{\mathrm{DI}}(E_1, \Omega_1, \Omega_2)\delta(E_0 + N\hbar\omega - E_1 - E_2)\,, \qquad (111)$$

where E_0 is the ground-state energy. It is worthwhile to mention that unlike the joint two-electron energy distribution, the TDCS as calculated by (110) is, within reasonable limits, insensitive to the pulse shape used in the time-dependent approach since the Fourier width of the pulse is accounted for by the integration over the energy of the second electron.

Instead of specifying one of the energies and integrating over the other, it is also possible to specify energy (or momentum) sharing. For that purpose, we transform from the usual coordinates (E_1, E_2) to $(E_{\mathrm{tot}}, \alpha)$, with $E_{\mathrm{tot}} = E_1 + E_2$ and $\tan(\alpha) = E_1/E_2$. For a fixed value of α, the integration is performed over the total energy E_{tot}, i.e., along straight lines through the origin in Fig. 4. This results in the TDCS at fixed energy sharing (the frequently investigated case of equal energy sharing corresponds to $\alpha = \pi/2$).

5.6 *Remarks on Two Photon Direct and Sequential Ionization of* He

Two-photon double ionization (TPDI) of helium is one of the simplest multiphoton processes involving electron correlation. Consequently, TPDI of atomic helium has been the subject of intense theoretical studies in the past few years [45–47, 63–108, 114, 150]. Most of the existing literature deals with either (i) cross sections

in the *nonsequential* regime of TPDI, or with (ii) the effects of ultrashort (attosecond) XUV pulses in the *sequential* regime of TPDI. Although the cross sections for nonsequential TPDI have attracted a significant amount of interest by theoreticians, the published results show large discrepancies. However, in the last few years, agreement has been observed between some quite different approaches for which the convergence has been extensively tested [45, 98, 106]. There are much fewer experimental studies as of yet, all of which are concerned with the nonsequential regime [99, 109–112]. For these, the experimental uncertainties are still too large to help in resolving the discrepancies in the theoretical results.

Calculations for two-photon ionization employ either a time-independent (TI) or a time-dependent (TD) approach. TI methods involve either lowest-order perturbation theory (LOPT) or R-matrix Floquet theory, and are only applicable in the limit of (infinitely) long pulses. TD methods are based on a direct solution of the time-dependent Schrödinger equation and are therefore not restricted to any given order of the perturbation or pulse duration. The results we present in the following are mostly calculated at moderate intensities of the XUV field ($\sim 10^{12}\,\mathrm{W/cm^2}$). At this intensity, corrections to LOPT are expected to be small. The decisive advantage of TD methods here stems from a different aspect. Namely, TI calculations of processes involving correlated two-electron final states in the continuum, $\Psi_{\mathbf{k}_1,\mathbf{k}_2}(\mathbf{r}_1,\mathbf{r}_2)$, require the knowledge of the final state in the entire configuration space in order to calculate the two-photon transition amplitude $t^{(2)}_{i\to\mathbf{k}_1,\mathbf{k}_2}$. As the numerical or analytical determination of accurate correlated continuum final states remains a challenge, evaluation of $t^{(2)}_{i\to\mathbf{k}_1,\mathbf{k}_2}$ involves, inevitably, additional approximations that are difficult to control. Adding the time as an additional degree of freedom to the six spatial dimensions of the two-electron problem allows one to bypass the determination of $\Psi_{\mathbf{k}_1,\mathbf{k}_2}$. Instead, we propagate the wave packet for sufficiently long times such that we can extract the relevant dynamical information entirely from the asymptotic region where electron correlations become negligible. Moreover, residual errors can be controlled by systematically varying the propagation time. This advantage comes along with a distinct disadvantage: Results will, in general, depend on the time-structure imposed on the external perturbation, specifically on the duration and temporal shape of the XUV pulse. A comparison with TI calculations on the level of (generalized) cross sections therefore requires a careful extraction of information and checks of the independence from pulse parameters.

5.7 *Sequential and Nonsequential Regimes of TPDI*

The nature of the two-photon double ionization (TPDI) process depends strongly on the photon energy $\hbar\omega$. In order to doubly ionize the helium atom, $\hbar\omega$ has to be large enough so that two photons can fully ionize the atom, i.e., $2\hbar\omega > I_1 + I_2 = -E_0$, where $I_1 \approx 24.6\,\mathrm{eV}$ and $I_2 \approx 54.4\,\mathrm{eV}$ are the first and second ionization potential of helium, while $E_0 \approx -79\,\mathrm{eV}$ is the total ground-state energy. In a "long" pulse with an approximately delta-like energy spectrum, there are two distinct regimes of

TPDI, depending on the photon energy. In "real" pulses with finite spectral width, the photon energy is described by a distribution $\mathcal{F}(\omega)$. The following arguments thus depend on the assumption that the width of that distribution is sufficiently small for the regime to be identified unambiguously.

For $\hbar\omega > I_2$, one photon has enough energy to ionize the He^+ ion in its ground state. In this regime, an independent-particle picture is applicable: each electron absorbs one photon and electron-electron interaction is a priori not required for double ionization to occur. Therefore, the double ionization can proceed in two well-separated steps, and this energy regime is called the *sequential* regime. The first electron is ejected with energy $E_1 = \hbar\omega - I_1$, carrying with it the energy contained in the electron-electron interaction in the ground state. At a later time, when the first electron is well separated from the remaining ion, the second electron is ejected with the energy $E_2 = \hbar\omega - I_2$. In long pulses, this is the dominant process, leading to an electron energy spectrum with two sharp peaks at E_1 and E_2. In the limit of low pulse intensities, where depletion can be neglected, the total yield is proportional to the square of the pulse duration ($P_{\text{seq}}^{\text{DI}} \propto T^2$), taken to be the signature of the sequential (two-step) nature of the process.

For high photon energies, different sequential pathways become accessible. The first photon absorption can produce *shake-up* in the remaining He^+ ion, leaving it in an excited state, with the second absorption proceeding from this excited state. These pathways are accessible for the sequential process when one photon provides enough energy to strip one electron from the atom and simultaneously excite the ion to a higher state, i.e., if $\hbar\omega > I_1 + \mathcal{E}_n$, where $\mathcal{E}_n = (2 - 2/n^2)$ a.u. is the excitation energy to the nth shell of the He^+ ion. In long pulses and for high photon energies, this leads to shake-up satellite lines in the electron energy spectrum [151]. While the first ionization potential is increased for shake-up ionization, the second ionization potential is decreased ($I_2' = I_2/n^2$). Consequently, the peak positions $E_1' = \hbar\omega - I_1 - \mathcal{E}_n$, $E_2' = \hbar\omega - I_2 + \mathcal{E}_n$ are different from those without shake-up, but the overall picture of sequential and independent photoionization events remains unchanged. There are, however, two reasons why some correlation between the electrons can be expected even for long pulses: for one, the electron that is emitted later is *faster* than the first electron in the shake-up pathway. If the electrons are emitted in the same direction, the second electron can thus collide with the first one, modifying the independent-particle behavior. In addition, the excited states of the He^+ ion are (almost) degenerate in angular momentum, such that the He^+ ion can remain in a superposition of excited states, with the coefficients depending on the emission angle of the first electron. This can also cause nonvanishing angular correlation between the electrons even in very long pulses. As the photon energy approaches the threshold for one-photon double ionization at $\hbar\omega = -E_0$, successively higher shake-up states become accessible. However, the probability for shake-up quickly decreases with the quantum number n of the intermediate excited state, such that typically, only the first few excited states play a role even if more are energetically accessible.

If the photon energy $\hbar\omega$ is smaller than the second ionization potential I_2, the sequential process can not occur. The two photons still provide enough energy to

doubly ionize the helium atom, but only if the two electrons share the available energy. This regime is called the *nonsequential* regime. This implies that the process can only happen if both photons are absorbed almost simultaneously. The two consequences of this are that the energy of the intermediate state, which is only populated transiently, does not need to be $\hbar\omega + E_0$ (because of the quantum mechanical time-energy uncertainty), and that the electrons can interact and exchange energy. Consequently, the asymptotic energies of the electrons in the final state do not have to be $E_1 = \hbar\omega - I_1$ and $E_2 = \hbar\omega - I_2$ (where for $\hbar\omega < I_2$, E_2 would be negative and therefore not correspond to a free electron). Because the photons have to be absorbed quasi-simultaneously, the total double ionization yield in the nonsequential regime is linearly proportional to the pulse duration, $P^{\mathrm{DI}}_{\mathrm{nonseq}} \propto T$ as long as depletion can be neglected.

It should be stressed that even in the sequential spectral regime, there are nonsequential contributions to the total double ionization which can be identified by their linear scaling with T. In particular, final states where the electron energies are not at the sequential peaks are only reached by nonsequential processes.

5.8 *Results on Two Photon Direct Ionization of* He

In Fig. 6, we compare the present results for the total cross section with various published data. In order to achieve converged values, the spectral bandwidth of the laser pulse used to calculate the cross section (according to (108)) has to be sufficiently small. The spectral width of the pulse depends both on the pulse shape as well as on the total duration of the pulse. The laser pulses had a $\sin^2$ envelope, defined by

$$f(t) = \begin{cases} \sin^2\big((\pi/T)t\big) & 0 < t < T, \\ 0 & \text{otherwise.} \end{cases} \tag{112}$$

As the threshold for sequential TPDI is approached, successively longer pulses are necessary to resolve the rapidly growing cross section. The present results in Fig. 6(a) were obtained with 4 fs pulses for $\hbar\omega \leq 51$ eV, 11 fs pulses for $\hbar\omega \leq 53$ eV and 20 fs pulses for $\hbar\omega = 53.5$ eV and $\hbar\omega = 54$ eV. The calculations were performed with different box sizes depending on the pulse duration, with $r_{\max} = 240$ a.u. for the smallest boxes and $r_{\max} = 1400$ a.u. for the largest boxes. The FEDVR elements contained 11 basis functions each and spanned 4–4.4 a.u.. The maximum angular momentum values used were $L_{\max} = 3$ for the total angular momentum and $l_{1,\max} = l_{2,\max} = 7$ for the individual angular momenta. The peak intensity was chosen as $I_0 = 10^{12}\,\mathrm{W/cm^2}$. The ionization yields were extracted at least 1 fs after the pulse. The projection error should be less than 2% [45].

For photon energies below around 50 eV, the total cross section for TPDI is a relatively smooth function of photon energy, showing an approximately linear increase. Above the threshold for sequential TPDI (54.4 eV), the cross section is not defined, as the yield then scales with the square of the pulse duration, whereas a cross sec-

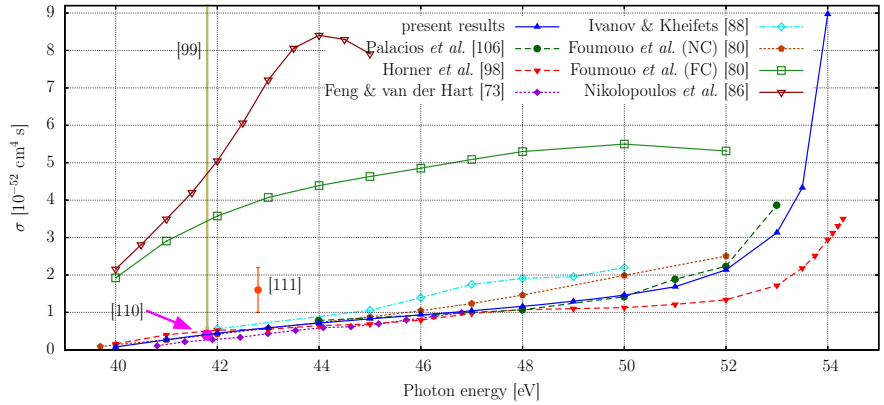

(a) Longest available pulses

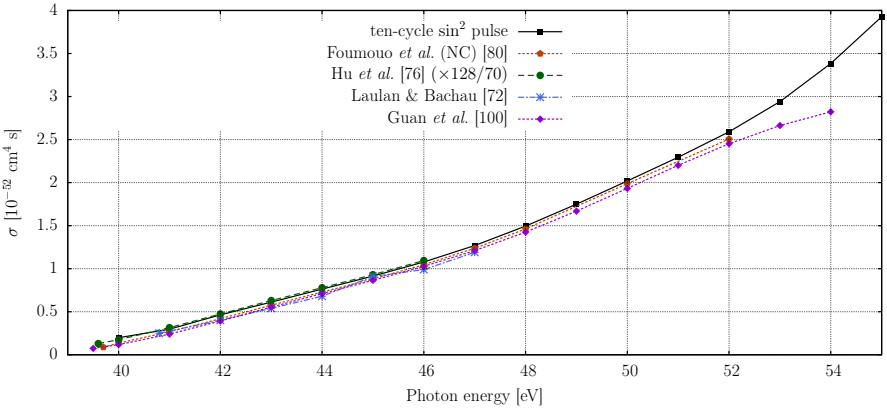

(b) Ten-cycle pulses

Fig. 6 Comparison of the total two-photon double ionization (TPDI) cross sections, obtained from (108), with $T_{\text{eff}} = 35T/128$. In (a), "present results" labels the data obtained with the longest $\sin^2$ pulse that we calculated at each energy (see text), all with a peak intensity of $10^{12}\,\text{W/cm}^2$. For the results of Foumouo et al. [80], (NC) labels the results obtained by projecting onto uncorrelated Coulomb waves, while (FC) labels the results obtained using the J-matrix method. (b) shows the results obtained with ten-cycle pulses compared to other approaches using the same pulses. The results of Hu et al. [76] were rescaled by a factor of $128/70$ in order to include the correct T_{eff}.

tion requires linear scaling with pulse duration. In order to extract the cross section close to the threshold, it is therefore necessary to ensure that the spectral width of the pulses is small enough such that the total yield only contains negligible contributions from the sequential process. By using successively longer pulses, we were able to resolve the threshold behavior up to less than one eV below the threshold, with the result for 53.5 eV being converged for $T = 20\,\text{fs}$. In order to resolve the behavior for energies even closer to the threshold, still longer pulses would have to

be used, which becomes prohibitively expensive. Close to the sequential threshold, the sequential process is *almost* possible and the electrons only have to exchange very little energy, leading to the observed rise in the cross section. This has been called the signature of the "virtual" sequential process [93].

The present results show a more pronounced variation with photon energy than other results obtained by direct integration of the time-dependent Schrödinger equation. This can be easily explained by the fact that most previous work employed ten-cycle pulses. At photon energies of 42–54 eV, this corresponds to about 1 fs total duration, and consequently, a spectral width (FWHM) of about 6 eV (for $\sin^2$ pulses). The results are therefore an average over a rather large energy window. In contrast, we use pulses of up to 20 fs duration with a narrower spectrum (FWHM $\sim$ 0.3 eV). To facilitate comparison with previous calculations, we have also performed a calculation using ten-cycle pulses (Fig. 6(b)) for which we indeed find better agreement. The pulse duration dependence becomes, in particular, critical near the threshold for sequential ionization at 54.4 eV.

We compare our results with data from both time-dependent and time-independent approaches. Laulan and Bachau [72] solved the TDSE by means of a B-spline method and an explicit Runge–Kutta propagation scheme. The double ionization probability was obtained by projecting onto uncorrelated Coulomb functions. They also included first-order correction terms in the representation of the double continuum (thus partly taking into account radial correlations). However, they found little difference with respect to the uncorrelated functions, as expected from our investigations. Hu, Colgan, and Collins [76] solved the time-dependent close-coupling equations using finite-difference techniques for the spatial discretization and the real-space product formula as well as a leapfrog algorithm for temporal propagation. The double ionization probability was also extracted by projection onto uncorrelated Coulomb waves. Guan, Bartschat and Schneider [100] used an approach very similar to ours, employing the FEDVR and using the Lanczos method for time propagation. Palacios et al. [106] also used an FEDVR basis, combined with a Crank-Nicholson time propagator. They extracted the double ionization yields by application of exterior complex scaling (ECS) and a formal propagation to $t \to \infty$. The volume integral for extraction of the momentum distribution can then be rewritten as a surface integral, performed at asymptotic distances to the core. The resulting amplitudes thus also include correlation.

Foumouo et al. [80] employed a spectral method of configuration interaction type (involving Coulomb–Sturmian functions) and an explicit Runge–Kutta time propagation to solve the TDSE. The double ionization probability is calculated by closure, i.e., by subtracting the singly ionized states from the total wave function and taking the remaining probability as the double ionization probability. The singly ionized states were constructed by using the J-matrix method, which should contain angular and radial correlations to the full extent (labeled FC in Fig. 6). In addition, they also performed projection on the uncorrelated product of Coulomb waves (labeled NC in Fig. 6). The results of Ivanov and Kheifets [88] are based on the time-dependent convergent close-coupling (CCC) method, taking into account correlations in the

final state to some degree. Nikolopoulos and Lambropoulos [86] solved the TDSE using an expansion in correlated multichannel wave functions.

Within the time-independent methods, Nikolopoulos and Lambropoulos [68] applied lowest-order non-vanishing perturbation theory (LOPT) to determine the generalized cross sections. Feng and van der Hart [73] employed R-matrix Floquet theory in combination with B-splines basis sets. The data from Horner et al. [93, 98] also result from LOPT calculations. They solved the Dalgarno–Lewis equations for two-photon absorption in LOPT employing exterior complex scaling (ECS) and also account for correlation in initial, intermediate, and final states.

Overall, our results are in reasonable to good agreement with those of [72, 73, 76, 80, 98, 100, 106] while sizable discrepancies exist in comparison with those of [68, 86] as well as those of [80] in which corrections due to final-state correlations are included. Clearly, the degree of convergence of the present results on the few percent level preclude any change of cross section by a factor of $5 - 10$, which would be necessary to obtain values of the same magnitude as [68,80,86]. This conclusion can be supported by analyzing the radial wave packet without converting to momentum space (not shown, cf. [44, 45]). The only other calculations approaching the threshold for sequential TPDI are those by the Berkeley group [93, 98, 106], which also show the strong increase of the total cross section as the threshold is approached. In particular, the data of Palacios et al. [106] agree with ours almost perfectly up to 52 eV. The deviation at 53 eV can be explained by the fact that they used pulses of total duration $T = 3$ fs, while we used longer pulses up to $T = 20$ fs close to threshold.

The experimental values of Hasegawa, Nabekawa et al. [109, 110] at 41.8 eV and of Sorokin et al. [111] at 42.8 eV (cf. Fig. 6) are compatible with most of the theoretical data. Antoine et al. [99] provide an experimental lower bound for the cross section at 41.8 eV, which is right at the value of the cross section obtained by most time-dependent approaches. Due to the experimental uncertainties (e.g., the harmonic intensity in [109, 110] or the assumptions on the pulse shape and focusing conditions in [111]), the currently available data are not sufficient to strongly support or rule out any of the theoretical results.

We turn now to the triply differential cross section (TDCS), the quantity most sensitive to the level of the underlying approximations. The present results show qualitative agreement with the published data [76, 88, 98, 106], but there are some pronounced quantitative differences. While the prominent back-to-back emission lobe (anti-)parallel to the laser polarization direction is well reproduced in most calculations (Fig. 7), the angular distribution for less favored emission directions (e.g., $\theta_1 = 90°$) differs significantly from other calculations. One reason is the sensitivity to the partial wave expansion. In contrast to the *total* cross section, the TDCS needs a larger number of angular momentum combinations (L, l_1, l_2) in the expansion of the wave function to converge. In order to resolve angular correlations in the TDCS, it is necessary to use large expansions in single electron angular momenta. More specifically, good convergence of the TDCS is only reached for values as high as $l_{1,\max} = l_{2,\max} = 7$ (cf. [45]), which exceeds the angular momentum content of most other calculations [76, 88].

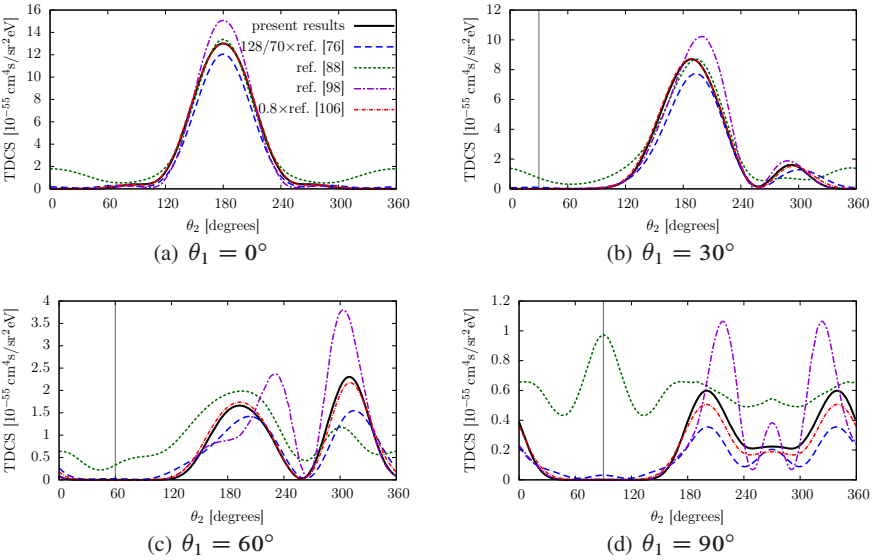

Fig. 7 Comparison of triply differential cross sections (TDCS) at 42 eV photon energy. Our data are obtained from (110), at $E_1 = 2.5$ eV, i.e., equal energy sharing, using a 4 fs $\sin^2$ laser pulse. In comparison, the results of Hu et al. [76], Ivanov and Kheifets [88], Horner et al. [98], and Palacios et al. [106] are shown. The vertical gray line shows the ejection angle θ_1 of the first electron. The angular momentum expansion used values of $L_{\max} = 4$ and $l_{1,\max} = l_{2,\max} = 9$. The radial box had an extension of 400 a.u., with FEDVR elements of 4 a.u. and order 11.

The data by Palacios et al. [106] were obtained from a 550 as pulse, for which the extracted total cross section is somewhat larger than in the converged case. After rescaling by a factor of 0.8 to account for this difference, the data agree almost perfectly with ours, owing to the fact that they used a similarly large angular momentum expansion. Horner et al. [98] solve the Dalgarno–Lewis equations for LOPT using an exterior complex scaling technique. In order to produce converged results, a small imaginary part has to be added to the photon energy in the first step of the calculation. The obtained results then have to be extrapolated to zero imaginary part, leading to some uncertainty in the relative phases of different contributions, which strongly influence the TDCS. Ivanov and Kheifets [88] take correlation in the final states into account using a convergent close-coupling (CCC) method. While the magnitude of their results is similar to those presented here, the shape differs considerably. In particular, they find significant probability for emission of both electrons in the same direction ($\theta_1 = \theta_2$), where the mutual repulsion of the electrons should be strongest. Foumouo et al. [105] calculated the TDCS for equal energy sharing at 45 eV photon energy using two different methods. The results obtained by projecting the final wave function on products of Coulomb waves resemble ours (not shown here for 45 eV, but the behavior is similar as for 42 eV). However, when correlation in the final state is taken into account using their J-matrix method, the results are

much larger in magnitude (as for the total cross section, cf. Fig. 6) and display a shape reminiscent of the one obtained by Ivanov and Kheifets [88], with the same surprising feature of emission in the same direction at equal energy sharing.

5.9 *Results on Two Photon Sequential Ionization of* He

The (two-photon) sequential ionization yield can be written as

$$P_{\text{seq}}^{\text{DI}} = \int_{-\infty}^{\infty} \mathrm{d}t\, \sigma_1 \Phi(t) \int_{t}^{\infty} \mathrm{d}t'\, \sigma_2 \Phi(t') \,, \tag{113}$$

where σ_1 is the one-photon cross section for single ionization of He, and σ_2 is the one-photon cross section for ionization of the He^+ ion. Using the symmetry of the integrand yields

$$P_{\text{seq}}^{\text{DI}} = \sigma_1 \sigma_2 \frac{1}{2} \left(\int_{-\infty}^{\infty} \mathrm{d}t\, \Phi(t) \right)^2 = \frac{\sigma_1 \sigma_2 I_0^2}{2\omega^2} (T_{\text{eff},1})^2 \,, \tag{114}$$

which is proportional to the square of the total pulse duration. It is therefore impossible to define a cross section in the usual sense and one needs to examine angular and energy distributions to understand the physical process at play. The effect of the duration of the laser pulse on the double ionization is shown in Fig. 8. In this part, we label the pulses by the FWHM of the electric field envelope, which is the more common value for ultrashort pulses.

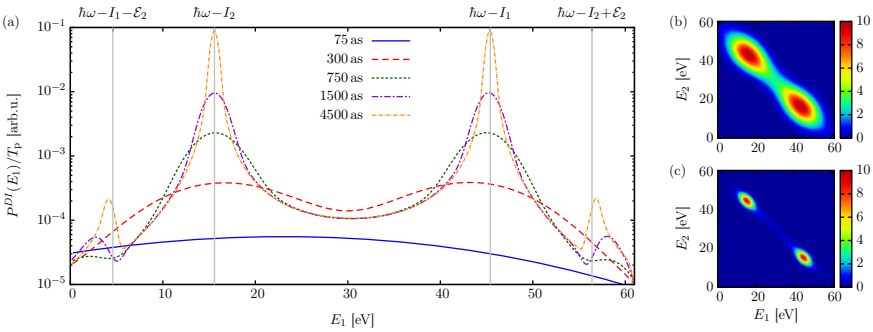

Fig. 8 (a) Double ionization (DI) rate $P^{\text{DI}}(E)/T$ (i.e., DI probability divided by the pulse duration) for TPDI by an XUV pulse at $\hbar\omega = 70\,\text{eV}$ with different FWHM pulse durations T. For sufficient pulse duration, the DI rate converges to a stable value except near the peaks of the sequential process, indicating a nonsequential process. Close to the energies of the shake-up peaks, the Fano-like structures indicating interference between the sequential and nonsequential contributions can be observed. (b) and (c) show the two-electron energy spectrum $P^{\text{DI}}(E_1, E_2)$ for (b) $T = 300\,\text{as}$ and (c) $T = 750\,\text{as}$.

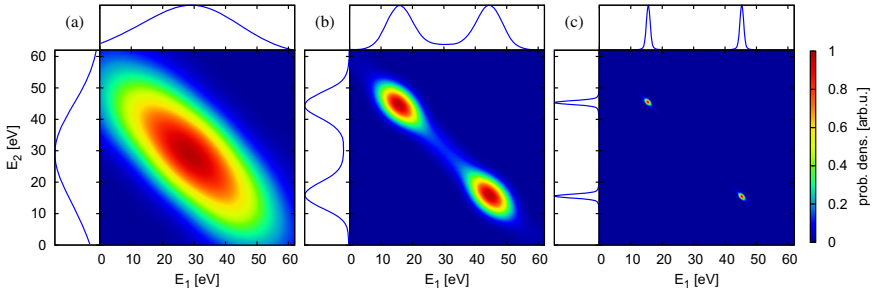

Fig. 9 Two-photon double ionization electron spectra $P^{\mathrm{DI}}(E_1, E_2)$ at 70 eV photon energy for different pulse durations: (a) 150 as, (b) 450 as, (c) 3000 as FWHM. The sides show the spectrum integrated over either energy, i.e., the one-electron energy spectra $P^{\mathrm{DI}}(E_1) = P^{\mathrm{DI}}(E_2)$.

The effect of the pulse duration can be seen even more clearly in the joint probability $P^{\mathrm{DI}}(E_1, E_2)$ distribution in the plane of electron energies, This clearly reveals the breakdown of the sequential ionization picture with decreasing pulse duration (Fig. 9).

For long pulses ($T = 3$ fs), two distinct peaks signifying the emission of the "first" electron with energy $E_1 = \hbar\omega - I_1$ (with I_1 the first ionization potential) and the "second" electron with $E_2 = \hbar\omega - I_2$ are clearly visible.

Contributions from shake-up satellites with energies $E_1' = \hbar\omega - I_1 - \mathcal{E}_n$ and $E_2' = \hbar\omega - I_2 + \mathcal{E}_n$ are below the one-percent level and barely discernible. For pulses of the order of one hundred attoseconds a dramatically different picture emerges: The two peaks merge into a single one located near the point of symmetric energy sharing $E_s = \hbar\omega - (I_1 + I_2)/2$.

It should be noted that this is not simply due to the Fourier broadening of the pulse. Instead, the close proximity in time of the two emission events allows for energy exchange between the two outgoing electrons representing a clear departure from the independent-particle behavior. Differently stated, the time interval between the two ionization events is too short for the "remaining" electron to relax to a stationary ionic ground (or excited) state. In the limit of ultrashort pulses the notion of a definite time ordering of emission processes loses its significance, as does the distinction between "sequential" and "nonsequential" ionization.

The attosecond-pulse-induced dynamical electron correlation becomes more clearly visible in the joint angular distribution $P^{\mathrm{DI}}(\theta_{12}, \theta_1)$ (Fig. 10), where θ_1 is the polar emission angle of one electron, chosen in the following to coincide with the polarization axis of the XUV pulse ($\theta_1 = 0°$), and θ_{12} is the angle between the two electrons (here and in the following we choose coplanar geometry with $\phi_1 = \phi_2 = 0$). In the limit of "long" pulses ($T \gtrsim 3$ fs), the joint angular distribution is the product of two independent Hertz dipoles, each of which signifies the independent interaction of one electron with one photon. Consequently, also the conditional angular distribution $P^{\mathrm{DI}}(\theta_{12}, 0)$ corresponds to a Hertz dipole. With decreasing pulse duration, $P^{\mathrm{DI}}(\theta_{12}, 0)$ displays strong deviations and develops a pro-

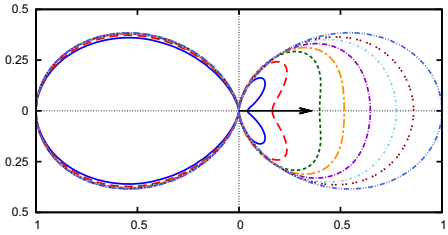

Fig. 10 Conditional angular distributions $P^{\mathrm{DI}}(\theta_{12}, \theta_1)$ at $\theta_1 = \phi_1 = \phi_2 = 0°$ of ejected electrons for different pulse lengths at 70 eV photon energy. The innermost (solid blue) line is for 75 as FWHM pulse duration, with successive lines for 150 as, 300 as, 450 as, 750 as, 1500 as, and 3000 as FWHM pulse duration. The outermost line is the dipolar ($\cos^2(\theta_1)$) distribution expected in the independent-particle limit of very long pulses. The distributions have been normalized to a maximum value of one for better comparison.

nounced forward-backward asymmetry. The conditional probability for the second electron to be emitted in the same direction as the first is strongly suppressed. For T of the order of a hundred attoseconds, the two electrons are emitted back to back. It is worth noting that the strong preference for emission in opposite directions persists after integration over the emission energies. Nevertheless, approximately equal energy sharing dominates (see Fig. 9). Thus, the dominant break-up mode induced by an attosecond pulse corresponds to ejection of the two electrons at 180 degrees, the so-called "Wannier ridge" configuration [152].

It is now instructive to inquire into the strong electron correlation observed for short pulses. Three different sources can be distinguished:

(i) Initial-state correlations in the helium ground state. Due to Coulomb repulsion, the electrons in the ground state are not independent of each other. For extremely short pulses, two-photon double ionization can thus be interpreted as a pump-probe setup that maps out the position (and momentum) of the second electron before it has time to relax to a spherically symmetric one-electron state.

(ii) Induced dipole polarization in the intermediate bound-free complex. When the first electron leaves the core, its electric field induces polarization of the remaining ion, leading to an asymmetric probability distribution of the second electron.

(iii) Final-state electron-electron interaction in the continuum. After the second electron has been released within the short time interval T as well, the mutual repulsion may redirect the electrons towards a back-to-back configuration.

While the dividing line between those mechanisms is far from being sharp, the present time-dependent wave packet propagation allows to shed light on their relative importance since they occur on different time scales. Relaxation of the ground-state correlations (i), i.e., of the deviation of the joint angular distribution $P^{\mathrm{DI}}(\Omega_1, \Omega_2)$ from a product of two spherically symmetric distributions is expected to occur on the time scale of the orbital period of the residual electron. As the re-

maining one-electron wave function will be mostly in the $n = 1$ and $n = 2$ shells, the uncertainty principle shows that the relevant timescale is approximately 16 as. Therefore, ground-state correlations will become clearly visible only for pulses with durations much shorter than one hundred attoseconds, shorter than those investigated here. The time scale for induced dipole polarization (ii) can be estimated by the time the first electron takes to escape to a distance larger than the radial extent of the residual wave function forming a dipole ($\langle r \rangle \approx 3$ a.u. in $n = 2$). Choosing a somewhat arbitrary distance of 10 a.u., the time necessary for the first electron to reach this distance after absorbing a 70 eV photon is about 120 as and thus of the order of the pulse lengths T considered. For higher photon energies, the first electron escapes to the same distance in a shorter time, decreasing the importance of this effect. In order to verify this, we have performed calculations at photon energies of 70, 91, 140, and 200 eV for a pulse duration of 75 as FWHM. Fig. 11(a) demonstrates that for higher energies, the asymmetry of the joint angular distribution is indeed strongly reduced.

Long-range Coulomb interactions in the continuum (iii) extend over much longer timescales which also strongly depend on the relative emission angles and energies of the electrons, i.e., $|\mathbf{k}_1 - \mathbf{k}_2|$. For example, for two electrons ejected in the same direction and with similar energies, the interaction will last much longer than for ejection in opposite directions. This can be verified by using an ultrashort pulse to start a two-electron wave packet in the continuum and observing the evolution of the joint angular distribution after the laser pulse is switched off (Fig. 11(b)). Directly after the pulse, the distribution of the electrons shows a decreased probability for ejection on the same side of the nucleus (primarily because of (ii)), but the lobes in forward and backward direction still mostly retain the shape expected from a dipole transition. As continuum final-state interactions persist, the joint angular distribution develops a pronounced dip at equal ejection angle as time passes. The change at larger relative angles is almost negligible.

One remarkable feature of the conditional angular distribution is the persistence of the nodal plane at $\theta = 90°$. While correlation effects strongly perturb the shape

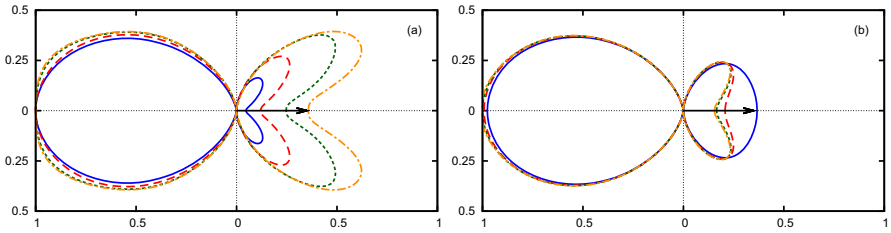

Fig. 11 Conditional angular distributions of ejected electrons after an XUV pulse. (a) For a duration (FWHM) of 75 as for different photon energies. From inside to outside: 70 eV, 91 eV, 140 eV, and 200 eV. The amount of asymmetry decreases with increasing pulse energy. (b) For different times after a 150 as (FHWM, total duration 300 as) pulse at 70 eV photon energy. The times (from the outermost to the innermost line) are 25 as, 350 as, 1000 as, and 1800 as after the end of the pulse.

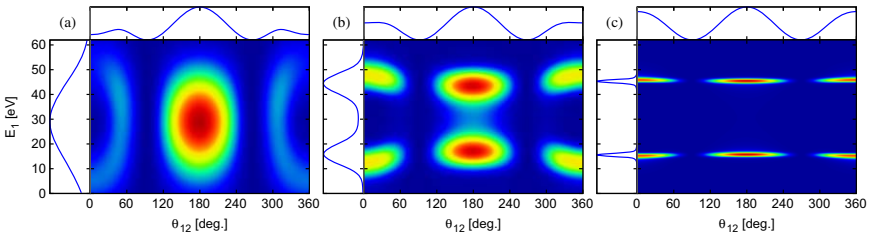

Fig. 12 Angle-energy distribution $P^{\mathrm{DI}}(E_1, \theta_{12}, \theta_1 = 0°)$ in coplanar geometry at 70 eV photon energy for different pulse durations: (a) 150 as, (b) 450 as, (c) 3000 as FWHM. The side plots show the distribution integrated over, respectively, energy and angle.

of the independent-particle dipolar shape, the nodal plane expected for the angular distribution of two electrons absorbing one photon each is approximately preserved. This is in contrast to one-photon double ionization, where necessarily only one electron absorbs energy from the photon and electron ejection at normal angle to the polarization axis is indeed observed [67, 153, 154].

Additional insights can be gained from a different projection of the two-electron momentum space distribution onto the energy-angle plane,

$$P^{\mathrm{DI}}(E_1, \theta_{12}, \theta_1 = 0°) = \int P^{\mathrm{DI}}(E_1, E_2, \Omega_1, \Omega_2)\, \mathrm{d}E_2 \,, \tag{115}$$

in coplanar geometry ($\phi_1 = \phi_2 = 0°$) and for $\theta_1 = 0°$. While for long pulses the energy of the emitted electrons (E_1) is independent of the relative emission angle (Fig. 12(c), strong energy-angle correlations develop for short ($T \leq 500$ as) pulses. The dominant emission channel is the back-to-back emission at equal energy sharing ($E_1 \approx 30$ eV). This corresponds precisely to the well-known Wannier ridge riding mode [152], previously observed in e-2e ionization processes [155] and also invoked in the classification of doubly-excited resonances [156]. Because of the large instability of the Wannier orbit its presence is more prevalent in break-up processes than in quasi-bound resonances. A second subdominant but equally interesting channel opens for short pulses at $\theta_{12} = 0°$, i.e., emission in the same direction. One of the electrons is slowed down while the other one is accelerated, i.e., the fast electron is "pushed" from behind by the slower electron. The slower electron thus transfers part of the energy absorbed from the photon field to the faster electron. This is the well-known *post-collision interaction* [157–159] first observed by Barker and Berry in the decay of autoionizing states excited through ion impact [160].

6 H_2^+

6.1 *Introduction*

The question of the validity of the Born-Oppenheimer approximation when molecules are exposed to ultrashort laser pulses is of considerable interest. For molecules containing more than one electron, the situation can become exceedingly complex as the absorption of photons, the relative energies of the electrons, the electronic interaction and the nuclear motion play against one another in a subtle manner. For a one electron molecule, H_2^+, there are many simplifications. Since only one electron is ejected, the inter-electronic aspects of the ionization are not present and the question reduces to whether the electron can escape from the molecular core sufficiently quickly that the absorption of the photons and the dynamics of the nuclei are basically decoupled. Clearly, if the electron is ionized with very small kinetic energy, there is the possibility of significant nonadiabatic effects. Conversely, if the electron moves out of the interaction region rapidly, the nuclei are likely to impulsively fly apart and be governed primarily by simple classical dynamics. To examine this question, the four dimensional (x, y, z, R), time-dependent Schrödinger equation (TDSE) was solved using the FEDVR/Real-Space-Product (RSP) technique [135], including the dynamical motion of the nuclei.

Specifically, we exposed the target to linearly polarized light at arbitrary angles with respect to the molecular axis. Calculations were performed at different angles and photon energies ($\hbar\omega = 50\,\text{eV}$–$630\,\text{eV}$) to investigate the energy and orientation dependence of the photoionization probability [50, 161]. While we have not yet seen any major evidence of non-Born–Oppenheimer behavior, we have uncovered some quite interesting physics. At a photon energy of $\hbar\omega = 50\,\text{eV}$, there is a strong orientation dependence of the photoionization probability of H_2^+. At this energy, the ejected photoelectron is emitted "tilted" with respect to the molecular axis. This ionization anisotropy then appears to vanish at higher photon energies ($\hbar\omega \geq 170\,\text{eV}$). When these higher-energy XUV pulses are polarized perpendicular to the internuclear axis, a "double-slit-like" interference pattern is observed. However, we find that the diffraction angle only approaches the classical formula $\phi_n = \sin^{-1}(n\lambda_e/R_0)$ when $n\lambda_e$ becomes less than 65% of the internuclear distance R_0, where n is the diffraction order and λ_e is the wavelength of the released electron. The observations are explained by the different geometric "cross-sections" seen by the photo-ejected electron in the half-scattering process of leaving the molecule. The results illustrate the possibility of employing attosecond pulses to perform photoelectron microscopy of molecules.

6.2 *Results and Discussions*

6.2.1 The Ground State

As an initial condition, we choose the ground state of 4D H_2^+, determined using imaginary time (IT: $t \rightarrow i\tau$) propagation of (1). Under the transformation to imaginary time, an initial arbitrary wave packet will evolve into the ground-state wave function for sufficiently long propagation times. As shown in Fig. 13(a) and (b), the total energy and the expectation value of the internuclear distance $\langle R \rangle$ approach $E_0 \simeq -0.59$ a.u. and $\langle R \rangle \simeq 2.02$ a.u. respectively. The errors are within 2% of the analytical values ($E_0 \simeq -0.603$ a.u. and $\langle R \rangle \simeq 2.00$ a.u.). The ground-state probability density is plotted in the xy-plane and the xR-plane in Fig. 13(c) and (d), with the internuclear distance along the x-axis.

6.2.2 Photoionization Anisotropy

We first consider linearly-polarized, attosecond XUV pulses in the xy-plane at a photon energy of $\hbar\omega = 50$ eV at any angle θ with respect to the molecular axis R. The driving radiation is a $\sin^2$ pulse with a total duration of 500 as and a field strength of about 0.53 a.u.. The case of $\theta = 0°$ ($\theta = 90°$) corresponds to the laser polarization parallel (perpendicular) to the molecular axis. Figure 14 traces the dy-

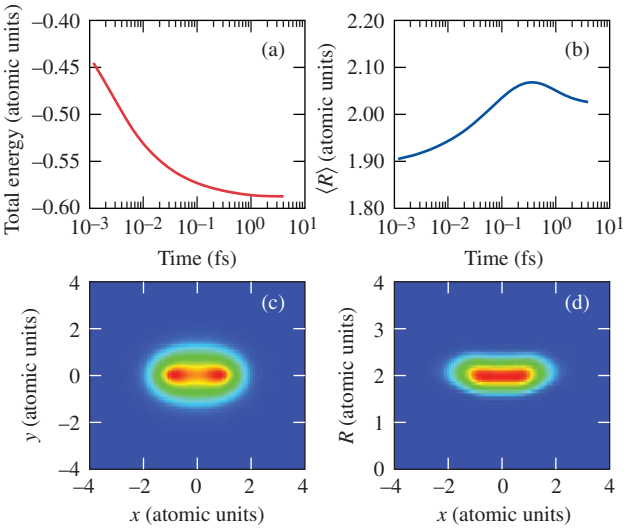

Fig. 13 The ground state of 4D H_2^+ obtained from imaginary-time propagation: (a) The system energy as a function of the propagation time, (b) the expectation value of the internuclear distance $\langle R \rangle$ versus propagation time, (c) the probability density profile in the xy-plane, and (d) the probability density profile in the xR-plane.

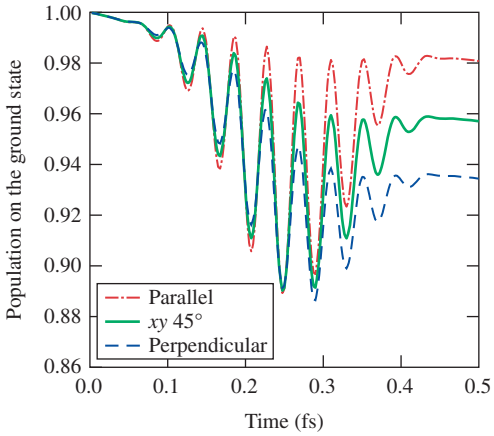

Fig. 14 Time-dependent ground-state population of H_2^+ driven by attosecond XUV pulses ($\hbar\omega = 50$ eV, $T = 500$ as) polarized parallel to the molecular axis [x-axis] (dash-dotted/red line), perpendicular to the molecular axis (dashed/blue line), and at $\theta = 45°$ relative to the molecular axis in the xy-plane (solid/green line), respectively. A strong orientation dependence of the ground-state depletion is observed for such conditions.

namics of the ground-state population for three cases: parallel ($\theta = 0°$) [red/dash-dotted line], perpendicular ($\theta = 90°$) [blue/dashed line], and "tilted" ($\theta = 45°$) [green/solid line]. As the ground-state population is gauge-dependent, one has to be careful concerning the physical interpretation of features seen in the figures. We have chosen to use the length gauge, which typically shows much larger oscillations than the velocity gauge. The ground-state populations adiabatically follow the field variation due to polarization effects, but with a doubled frequency because both the positive and negative oscillations of the field polarize the ground state in the same way. At the end of the XUV pulse, we observe three times more ground-state depletion from the perpendicular as compared to the parallel orientation, with the "tilted" ($\theta = 45°$) case lying in between. While the intermediate polarization (the "dips") behaves similarly in all three cases, the ionization probabilities differ considerably. In the parallel case, the field-driven wave function returns almost entirely to the ground state. In the perpendicular configuration, the ground state is more strongly depleted, as shown by the continuously decreasing population peaks [blue/dashed line].

To better understand the dependency on orientation, we calculated the total energy change ($\langle H_0 \rangle - E_0$) while the pulse was interacting with the molecule. Figure 15 shows the results for the three cases. The high-frequency oscillations are a numerical artifact and should be ignored. The perpendicular orientation substantially enhances the energy exchange between the field and the molecule, yielding more than three times the energy absorption of the parallel ($\theta = 0°$) case. Greater energy absorption at $\theta = 90°$ implies a larger excitation/ionization probability, which is consistent with the larger ground-state depletion seen in Fig. 14.

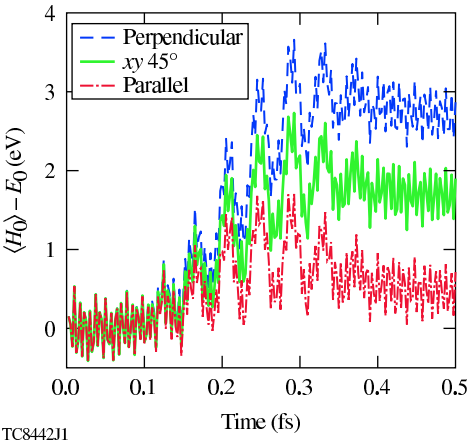

Fig. 15 The molecular system energy change $[\langle H_0 \rangle - E_0]$ during the attosecond pulse interaction ($\hbar\omega = 50$ eV, $T = 500$ as), for polarization parallel (dash-dotted/red line), perpendicular (dashed/blue line), and at 45° relative to the molecular axis in the xy-plane (solid/green line), respectively. Note, the very high frequency oscillations are a numerical artifact.

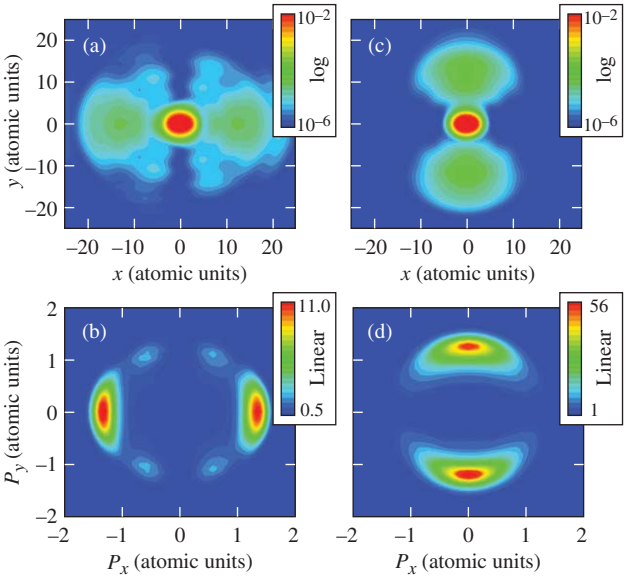

Fig. 16 Electron probability densities of H_2^+ at the end of the attosecond XUV pulse ($\hbar\omega = 50$ eV) for (a) polarization parallel to the molecular axis and (c) perpendicular to the molecular axis. The corresponding momentum distributions of the ejected photoelectrons are shown in (b) and (d), respectively. The ionization probability is three times higher for perpendicular polarization than for parallel polarization.

Snapshots of the probability density in the xy-plane of configuration space are plotted in Fig. 16(a) and (c) at the end of the XUV pulse for $\theta = 0°$ and 90°. The corresponding momentum distributions are shown in Fig. 16(b) and (d), respectively. By integrating the electron probability in regions greater than ~ 5 bohr from the molecular center, one finds, not unexpectedly, that the ionization probability

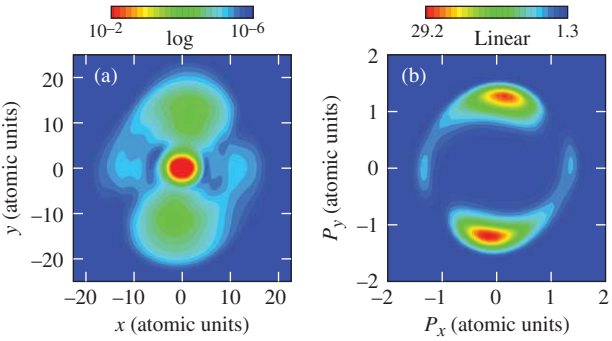

Fig. 17 (a) Pulse-ending snapshot of the electron probability density of H_2^+ for the case of "tilted" polarization ($\theta = 45°$) with respect to the molecular axis (x-axis); (b) corresponding photoelectron momentum distribution in the xy-plane. It is noted that the ejected photoelectron peaks off the polarization axis, which is a result of the orientation dependence of attosecond photoionization of H_2^+.

becomes more than three times higher in the perpendicular than the parallel case. Overall, the ejected electron momentum spectrum is dominated by single-photon absorption, i.e., a peak at $\hbar\omega - I_P = E_K \simeq 20\,\text{eV}$. Therefore, the observed ionization difference between orientations is independent of the XUV pulse intensity. Although electrons are ejected in line with the XUV pulse polarization for these two cases, slightly different features arise. For example, small-amplitude features appear at large angles in the parallel case [Fig. 16(a) and (b)], associated with the (half-)scattering of the electron between the two scattering centers. This feature is absent in the perpendicular case although the more extended distribution in the momentum spectrum may mask weak scattering signatures.

The orientation dependence of H_2^+ photoionization observed above has a consequence for a generally "tilted" pulse polarization in that the direction of electron ejection and the XUV polarization can differ. To illustrate this, we have plotted the probability density snapshots in Fig. 17(a) for the case of $\theta = 45°$ as well as the corresponding ionization momentum spectrum [Fig. 17(b)]. Instead of aligning with the XUV polarization direction, the probability density for the ejected electron now peaks at $\theta \simeq 82°$. The linearly-polarized field ($\theta = 45°$) can be equally decomposed into x- and y-components, for which the y-component of the field induces more ionization than the x-component. Thus, the overall ionization of the wave packet tends to "bend" toward the y-axis. Our calculations appear contrary to a recent XUV experiment of molecular tunneling ionization in H_2 in intense optical fields [162, 163] which found slightly more ($\sim 30\%$) ionization in the parallel orientation. We have also performed a few 4D calculations for HD^+ in the optical regime (not shown), which find behavior similar to that in the cited experiments. In the optical regime, the ejected electron has a wide range of energy from a few eV to a few hundred eV due to multiphoton ionization by the intense field. Very low-energy electrons have de Broglie-wavelengths much larger than the molecular size

and show no directional preference. On the other hand, when electron are ejected with high energy, ionization along the parallel polarization direction is slightly preferred. Thus, the overall tunneling ionization, given by the sum over all electron spectra, shows a less dramatic anisotropy than for single-photon ionization in the XUV regime.

To gain further insights into the orientation dependence of the ionization, we note that for a photon energy of $\hbar\omega = 50\,\text{eV}$, the ejected electron ($E_K \simeq 20\,\text{eV}$) has a de Broglie wavelength of $\lambda_e \simeq 5.2\,\text{bohr}$, more than twice the internuclear distance. Consequently, for the perpendicular direction (y-axis), the ejected electron cannot distinguish the two molecular centers and experiences a much larger geometrical cross-section for half-scattering than the case of parallel polarization. For the latter situation, the electrons always encounter aligned single-center half-scattering. We should therefore intuitively expect a more extended momentum distribution for perpendicular polarization. To characterize the extent of the momentum distribution, we take as a measure the angular spread Φ, estimated by the angle at which the probability drops to $1/e$ of its peak value. We find $\Phi \simeq 35°$ for perpendicular polarization, clearly exceeding $\Phi \simeq 24°$ for parallel polarization [cf. Fig. 16(b) and (d)]. A large cross section for scattering facilitates efficient photon absorption, thereby resulting in a higher ionization probability. If the above explanation is correct, such an orientation dependence of molecular photoionization should disappear once the de Broglie wavelength decreases (increasing $\hbar\omega$) sufficiently that the photoelectron can distinguish both scattering centers. At that point the half-scattering should take on a more uniform distribution. To test this hypothesis, we have performed calculations at $\hbar\omega = 170\,\text{eV}$ for both perpendicular and parallel polarizations with a 250 as XUV pulse but with a peak field strength of $\sim 3.76\,\text{a.u.}$ in order to get a noticeable ionization probability.

The results are shown in Figs. 18 and 19, respectively, for the ground-state depletion history and the total system energy change. From Fig. 18, we see that the final population left in the ground state is roughly similar for both situations although the parallel polarization results in a slightly higher ionization probability. A similar conclusion emerges from the field-molecule energy exchange as shown by Fig. 19.

Finally, we plot in Fig. 20(a) and (c) the probability density snapshots for the parallel and the perpendicular polarization cases, as well as the corresponding momentum distributions of the ionized electron wave packet in Fig. 20(b) and (d). We find that the ionization probability is roughly the same for these two cases and that the dramatic orientation dependence of H_2^+ photoionization, observed at the low photon energy of $\hbar\omega = 50\,\text{eV}$, disappears at $\hbar\omega = 170\,\text{eV}$. Once again, this is because the released "fast" electron ($E_K \simeq 140\,\text{eV}$) now has a de Broglie wavelength of $\lambda_e \simeq 1.96\,\text{bohr}$, which is slightly smaller than the internuclear distance. The ejected electron can now distinguish the two molecular "scattering" centers, with the consequence that the ionization no longer depends drastically on the direction of the ejected direction.

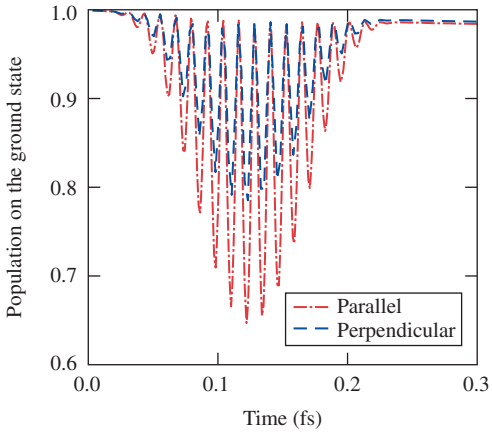

Fig. 18 Time-dependent ground-state population of H_2^+ driven by high photon-energy attosecond XUV pulses ($\hbar\omega = 170\,\text{eV}$), whose polarizations are either parallel (dash-dotted/red line) or perpendicular (dashed/blue line) to the molecular axis.

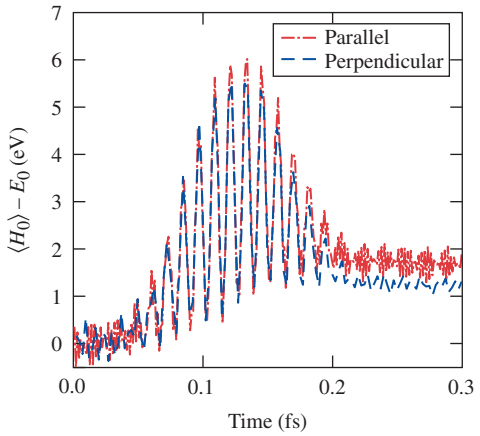

Fig. 19 Molecular system energy change $[\langle H_0 \rangle - E_0]$ versus the interaction time ($\hbar\omega = 170\,\text{eV}$), for parallel polarization (dash-dotted/red line) and perpendicular polarization to the molecular axis (dashed/blue line).

6.3 *Interference Effects*

We further examine the double-slit-like interference patterns that appear in perpendicular polarization [Fig. 20(b) and (d)]. All of the interference peaks reside within the momentum circle dictated by energy conservation ($E_K = \hbar\omega - I_P$). Basically, the photoelectron wave packet released from each center interfere, producing electrons ejected in specific directions. This behavior was discussed by Cohen and Fano almost a half a century ago [164]. More recently, Walter and Briggs [165], modeled

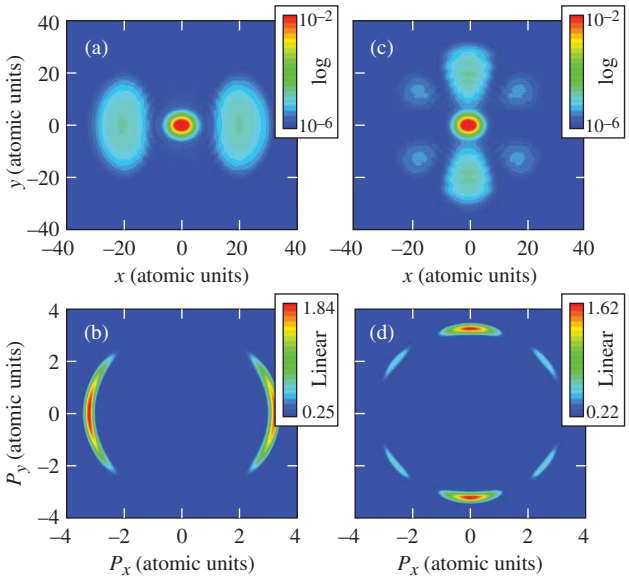

Fig. 20 Electron probability densities of H_2^+ at the end of the attosecond XUV pulses ($\hbar\omega = 170$ eV) for (a) polarization parallel to the molecular axis and (c) polarization perpendicular to the molecular axis. The corresponding momentum distributions of the ejected photoelectrons are shown in (b) and (d), respectively. The "double-slit-like" interference patterns are observed for the perpendicular polarization case. The orientation dependence of the yield in attosecond photoionization, observed at $\hbar\omega = 50$ eV, disappears in this case.

this phenomenon using time-independent methods within the Born-Oppenheimer approximation. Their calculations were performed at slightly larger photon energy ($\hbar\omega = 250$ eV) [166, 167] than the current calculations and were compared with measurements using circularly polarized light [168]. Our time-dependent results show that the first interference peak appears at an angle of $\phi \simeq 52°$ relative to the polarization y-axis. Young's double-slit formula, $R_0 \times \sin(\phi_n) = n\lambda_e$ used in time-independent studies [166], predicts the first peak at $\phi_1 \simeq 75°$ for the associated photon energy. Here, R_0 is the internuclear distance, λ_e is the de Broglie wavelength of the ejected electron, and n is the order of the interference peak. To examine the long-range Coulomb effects, we have freely propagated the wave packets to large distances (> 60 bohr) but still find the first interference angle little changed.

To resolve the discrepancy between our calculated diffraction angles and the predictions of the classical formula, we increased the photon energy of the XUV pulses from $\hbar\omega \simeq 210$ eV to 630 eV and performed a series of calculations, the results of which are shown in Table 1. We observe that the differences between the calculations and the classical formula decreases as the XUV photon energy increases. Above $\hbar\omega \simeq 350$ eV, the classical first-order diffraction angle (ϕ_1) is exactly recovered from our TDSE calculations. Two such examples are shown in Fig. 21(a) and (b), in which the electron probability densities are plotted for $\hbar\omega \simeq 350$ eV and

Table 1 The "double-slit" interference angles comparison between the "classical" double-slit (DS) formula and our TDSE calculations, as the photon energy ($\hbar\omega$) varies.

$\hbar\omega$ (eV)	λ_e (bohr)	Classical-DS angles (ϕ_n) (deg.)	TDSE angles (ϕ_n) (deg.)
170	1.9587	$\phi_1 \simeq 75.3°$	$\phi_1 \simeq 52.0°$
210	1.7274	$\phi_1 \simeq 58.5°$	$\phi_1 \simeq 49.5°$
250	1.5258	$\phi_1 \simeq 50.5°$	$\phi_1 \simeq 46.5°$
300	1.4104	$\phi_1 \simeq 44.1°$	$\phi_1 \simeq 42.3°$
350	1.2955	$\phi_1 \simeq 39.7°$	$\phi_1 \simeq 39.9°$
430	1.1588	$\phi_1 \simeq 34.9°$	$\phi_1 \simeq 34.8°$
630	0.9462	$\phi_1 \simeq 28.0°$	$\phi_1 \simeq 28.4°$
		$\phi_2 \simeq 69.1°$	$\phi_2 \simeq 60.7°$

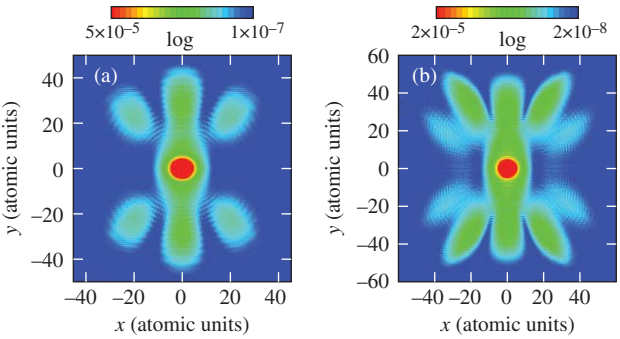

Fig. 21 The electron probability densities of H_2^+ at the end of the attosecond XUV pulses for polarization perpendicular to the molecular axis, for (a) $\hbar\omega = 350$ eV and (b) $\hbar\omega = 630$ eV. Different field strengths are applied in order to obtain noticeable ionization. Classical "double-slit" interference angles are recovered whenever $n\lambda_e \leq 65\% R_0$ is satisfied (see, more discussions in text).

$\hbar\omega \simeq 630$ eV, respectively. Interestingly, at the highest photon energy (630 eV), the second-order diffraction patterns appear. However, the resulting angle (ϕ_2) again disagrees with the classical double-slit prediction (see Table 1) although ϕ_1 remains in good agreement with the classical formula. These results indicate that the validity of the classical double-slit prediction requires that $n\lambda_e \leq 0.65 R_0$. If the interference path difference ($n\lambda_e$) becomes comparable to the internuclear distance R_0, the paths are no longer independent, and the classical double-slit condition ($\lambda \ll d$, where d is the separation of two slits) is not satisfied. e We conclude that the results of our calculations could guide the proper choice of photon energy for attosecond photoelectron imaging.

Finally, to have a sense of the energy sharing between the electron and the nuclei during the attosecond ionization, we computed the nuclear momentum spectrum for the wave packets associated with the ionized electron. The result, presented in Fig. 22 for the parallel polarization cases with two different field strengths $E = 0.53$ a.u. and $E = 0.053$ a.u. at $\hbar\omega = 50$ eV, show a transfer of less than ~ 0.1 eV of

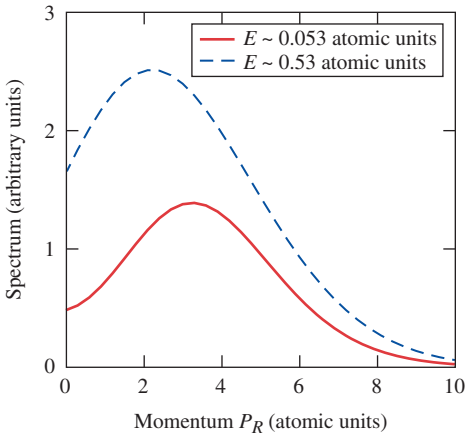

Fig. 22 The nuclear momentum spectrum for polarization parallel to the internuclear axis at $\hbar\omega = 50\,\text{eV}$.

photon energy to the nuclear motion during the attosecond photoionization process. The higher the field, the more "vertical" is the photoionization. The same behavior is also seen in the case of perpendicular polarization.

7 Summary

In conclusion, we have presented an overview of our numerical approaches to solve the time-dependent Schrödinger equation for two different three-body systems. We have demonstrated that these approaches provide detailed and reliable information about three-body breakup processes, both for the two-photon double ionization of He and the one-photon ionization (and break-up) of H_2^+.

7.1 *Helium*

In the case of helium, we have presented a detailed study of the dynamics of the two-photon double ionization process, for photon energies both in the nonsequential and sequential regime, and for a wide range of pulse durations (150 as to 9 fs). We have shown how electron-electron interaction, and thereby correlation, influences the observed energy spectra and angular distributions.

In particular, we have determined well-converged results for the total and triply differential (generalized) cross sections for nonsequential TPDI. Additionally, we have investigated the pulse duration dependence of the extracted cross sections. As the sequential threshold is approached, ever longer pulses are necessary to obtain converged values for the cross section.

For photon energies above the sequential threshold, the one-electron ionization rate $P^{\mathrm{DI}}(E)/T$ converges to a stable value with increasing pulse duration for electron energies away from the peaks associated with sequential ionization, giving rise to a well-defined (direct) differential double ionization cross section. Near the peaks, $P^{\mathrm{DI}}(E)/T$ grows with T. We have thus observed a nonuniform scaling of the double ionization probability with pulse duration.

If the photon energy is large enough to allow for shake-up ionization, i.e., ionization of He and simultaneous excitation of the remaining He^+ ion, a new kind of interference effect can be observed. In this spectral range, both the direct and sequential processes co-exist, giving rise to interferences which are induced by the short time correlation between the two emission events. This interference occurs between the nonsequential contributions of the channel without shake-up and the sequential shake-up channel, where the intermediate state after one-photon absorption is an excited state of the He^+ ion. In attosecond pulses, the channels can not be distinguished, while in long pulses (longer than the 9 fs used here), the sequential shake-up channel will dominate. For pulse durations of a few femtoseconds, as obtained in X-ray free-electron lasers, the two channels are similarly important, and the observed interference may allow one to measure the duration of ultrashort XUV pulses.

More information about the dynamics of the system is encoded in the angular distributions of the electrons. The electrons at the primary sequential peaks are essentially uncorrelated, while strong correlation is present for all other electron energies. Between the sequential peaks, i.e., close to equal energy sharing, the electrons are almost exclusively emitted in a back-to-back configuration. Outside the main peaks, the situation is reversed and the electrons are emitted preferentially in the same direction. For both of these cases, the two-lobed structure of a dipole transition from an *s* state is still visible, most clearly in the strong suppression of emission at an ejection angle of 90° to the laser polarization axis.

In addition, we have shown that attosecond XUV pulses can be used to probe, induce, and control electron correlation in two-photon double ionization. In such pulses, the scenario for "sequential" two-photon double ionization breaks down. Due to the small time interval between the two photoabsorption processes dynamical electron-electron correlations can be tuned by the pulse duration T. The angular and angle-energy distributions reveal the signatures of electronic correlation induced by the Coulomb interaction in the intermediate bound-free complex and in the final state with both electrons in the continuum. In ultrashort pulses, where the distinction between sequential and nonsequential processes breaks down, two well-known scenarios, the Wannier ridge riding mode and the post-collision interaction process, are simultaneously present in the two-electron emission spectrum. The favored emission channel is the Wannier ridge riding mode of back-to-back emission at equal energies.

7.2 H_2^+

We have investigated the attosecond XUV pulse ionization of H_2^+ by numerically solving the 4D time-dependent Schrödinger equation. Our results indicate that the single-photon ionization of H_2^+ has a strong orientation dependence at low photon energies, for which the released electron has a de Broglie wavelength much longer than the internuclear distance. The "half-scattered" electron sees a larger geometrical cross-section in the perpendicular direction, which therefore facilitates more ionization. With increasing photon energy, this photoionization anisotropy disappears due to the fact that the "fast" outgoing electron can distinguish the nuclear scattering centers. As a consequence, single-electron "double-slit-like" interference patterns emerge in the perpendicular polarization configuration. A series of calculations with high photon energies have been performed to explore the validity of the classical Young's double-slit condition. We found that to recover the diffraction angle (ϕ_n) predicted by the classical Young's double-slit formula, the identified condition of $n\lambda_e \leq 0.65R_0$ needs to be satisfied. Namely, the electron wavelength is required to be less than $\sim 65\%$ of the internuclear distance for the first diffraction angle to be same as the classical double-slit prediction, which guarantees each scattering pathway to be independent. These results provide a useful guide to attosecond photoelectron imaging of molecules. Finally, it is noted that the results from fixed-nuclei calculations (performed in 3D) are very similar to those from the current 4D calculations. This suggests that non-Born–Oppenheimer effects are negligible under the conditions used in this study. The capacity of our 4D code will be explored in the future by examining non-Born–Oppenheimer effects in intense field-molecule interactions.

Acknowledgements JF acknowledges support by the National Science Foundation through a grant to ITAMP. JF, SN, RP, and JB acknowledge support by the FWF-Austria, grants No. SFB016 and P21141-N16. The authors acknowledge the support of the NSF TeraGrid computational facilities at the Texas Advanced Computing Center (TACC) and at the National Institute for Computational Science (NICS), as well as computing time at the Vienna Scientific Cluster at the Vienna University of Technology and Institutional Computing resources at Los Alamos National Laboratory. The Los Alamos National Laboratory is operated by Los Alamos National Security, LLC for the National Nuclear Security Administration of the U.S. Department of Energy under Contract No. DE-AC52-06NA25396.

References

1. A.M. Kondratenko, E.L. Saldin, Particle Accelerators **10**, 207 (1980)
2. Y. Derbenev, A. Kondratenko, E. Saldin, Nucl. Instrum. Methods **193**, 415 (1982)
3. R. Bonifacio, C. Pellegrini, L.M. Narducci, Opt. Commun. **50**, 373 (1984)
4. J.B. Murphy, C. Pellegrini, Nucl. Instrum. Meth. A **237**, 159 (1985)
5. M.J. Hogan, C. Pellegrini, J. Rosenzweig, S. Anderson, P. Frigola, A. Tremaine, C. Fortgang, D.C. Nguyen, R.L. Sheffield, J.K. Wright, A. Varfolomeev, A.A. Varfolomeev, S. Tolmachev, R. Carr, Phys. Rev. Lett. **81**, 4867 (1998)

6. S.V. Milton, E. Gluskin, N.D. Arnold, C. Benson, W. Berg, S.G. Biedron, M. Borland, Y.C. Chae, R.J. Dejus, P.K. Den Hartog, B. Deriy, M. Erdmann, Y.I. Eidelman, M.W. Hahne, Z. Huang, K.J. Kim, J.W. Lewellen, Y. Li, A.H. Lumpkin, O. Makarov, E.R. Moog, A. Nassiri, V. Sajaev, R. Soliday, B.J. Tieman, E.M. Trakhtenberg, G. Travish, I.B. Vasserman, N.A. Vinokurov, X.J. Wang, G. Wiemerslage, B.X. Yang, Science **292**, 2037 (2001)
7. V. Ayvazyan, N. Baboi, I. Bohnet, R. Brinkmann, M. Castellano, P. Castro, L. Catani, S. Choroba, A. Cianchi, M. Dohlus, H.T. Edwards, B. Faatz, A.A. Fateev, J. Feldhaus, K. Flöttmann, A. Gamp, T. Garvey, H. Genz, Ch, V. Gretchko, B. Grigoryan, U. Hahn, C. Hessler, K. Honkavaara, M. Hüning, R. Ischebeck, M. Jablonka, Phys. Rev. Lett. **88**, 104802 (2002)
8. V. Ayvazyan, N. Baboi, J. Bähr, V. Balandin, B. Beutner, A. Brandt, I. Bohnet, A. Bolzmann, R. Brinkmann, O.I. Brovko, J.P. Carneiro, S. Casalbuoni, M. Castellano, P. Castro, L. Catani, E. Chiadroni, S. Choroba, A. Cianchi, H. Delsim-Hashemi, G. Di Pirro, M. Dohlus, S. Düsterer, H.T. Edwards, B. Faatz, A.A. Fateev, J. Feldhaus, K. Flöttmann, J. Frisch, L. Fröhlich, T. Garvey, U. Gensch, N. Golubeva, H.J. Grabosch, B. Grigoryan, O. Grimm, U. Hahn, J.H. Han, M.V. Hartrott, K. Honkavaara, M. Hüning, R. Ischebeck, E. Jaeschke, M. Jablonka, R. Kammering, V. Katalev, B. Keitel, S. Khodyachykh, Y. Kim, V. Kocharyan, M. Körfer, M. Kollewe, D. Kostin, D. Krämer, M. Krassilnikov, G. Kube, L. Lilje, T. Limberg, D. Lipka, F. Löhl, M. Luong, C. Magne, J. Menzel, P. Michelato, V. Miltchev, M. Minty, W.D. Möller, L. Monaco, W. Müller, M. Nagl, O. Napoly, P. Nicolosi, D. Nölle, T. Nuñez, A. Oppelt, C. Pagani, R. Paparella, B. Petersen, B. Petrosyan, J. Pflüger, P. Piot, E. Plönjes, L. Poletto, D. Proch, D. Pugachov, K. Rehlich, D. Richter, S. Riemann, M. Ross, J. Rossbach, M. Sachwitz, E.L. Saldin, W. Sandner, H. Schlarb, B. Schmidt, M. Schmitz, P. Schmüser, J.R. Schneider, E.A. Schneidmiller, H.J. Schreiber, S. Schreiber, A.V. Shabunov, D. Sertore, S. Setzer, S. Simrock, E. Sombrowski, L. Staykov, B. Steffen, F. Stephan, F. Stulle, K.P. Sytchev, H. Thom, K. Tiedtke, M. Tischer, R. Treusch, D. Trines, I. Tsakov, A. Vardanyan, R. Wanzenberg, T. Weiland, H. Weise, M. Wendt, I. Will, A. Winter, K. Wittenburg, M.V. Yurkov, I. Zagorodnov, P. Zambolin, K. Zapfe, Eur. Phys. J. D **37**, 297 (2006)
9. W. Ackermann, G. Asova, V. Ayvazyan, A. Azima, N. Baboi, J. Bähr, V. Balandin, B. Beutner, A. Brandt, A. Bolzmann, R. Brinkmann, O.I. Brovko, M. Castellano, P. Castro, L. Catani, E. Chiadroni, S. Choroba, A. Cianchi, J.T. Costello, D. Cubaynes, J. Dardis, W. Decking, H. Delsim-Hashemi, A. Delserieys, G. Di Pirro, M. Dohlus, S. Düsterer, A. Eckhardt, H.T. Edwards, B. Faatz, J. Feldhaus, K. Flöttmann, J. Frisch, L. Fröhlich, T. Garvey, U. Gensch, Ch, M. Görler, N. Golubeva, H.J. Grabosch, M. Grecki, O. Grimm, K. Hacker, U. Hahn, J.H. Han, K. Honkavaara, T. Hott, M. Hüning, Y. Ivanisenko, E. Jaeschke, W. Jalmuzna, T. Jezynski, R. Kammering, V. Katalev, K. Kavanagh, E.T. Kennedy, S. Khodyachykh, K. Klose, V. Kocharyan, M. Körfer, M. Kollewe, W. Koprek, S. Korepanov, D. Kostin, M. Krassilnikov, G. Kube, M. Kuhlmann, C.L.S. Lewis, L. Lilje, T. Limberg, D. Lipka, F. Löhl, H. Luna, M. Luong, M. Martins, M. Meyer, P. Michelato, V. Miltchev, W.D. Möller, L. Monaco, W.F.O. Müller, O. Napieralski, O. Napoly, P. Nicolosi, D. Nölle, T. Nuñez, A. Oppelt, C. Pagani, R. Paparella, N. Pchalek, J. Pedregosa-Gutierrez, B. Petersen, B. Petrosyan, G. Petrosyan, L. Petrosyan, J. Pflüger, E. Plönjes, L. Poletto, K. Pozniak, E. Prat, D. Proch, P. Pucyk, P. Radcliffe, H. Redlin, K. Rehlich, M. Richter, M. Roehrs, J. Roensch, R. Romaniuk, M. Ross, J. Rossbach, V. Rybnikov, M. Sachwitz, E.L. Saldin, W. Sandner, H. Schlarb, B. Schmidt, M. Schmitz, P. Schmüser, J.R. Schneider, E.A. Schneidmiller, S. Schnepp, S. Schreiber, M. Seidel, D. Sertore, A.V. Shabunov, C. Simon, S. Simrock, E. Sombrowski, A.A. Sorokin, P. Spanknebel, R. Spesyvtsev, L. Staykov, B. Steffen, F. Stephan, F. Stulle, H. Thom, K. Tiedtke, M. Tischer, S. Toleikis, R. Treusch, D. Trines, I. Tsakov, E. Vogel, T. Weiland, H. Weise, M. Wellhöfer, M. Wendt, I. Will, A. Winter, K. Wittenburg, W. Wurth, P. Yeates, M.V. Yurkov, I. Zagorodnov, K. Zapfe, Nat. Photonics **1**, 336 (2007)
10. P. Emma, R. Akre, J. Arthur, R. Bionta, C. Bostedt, J. Bozek, A. Brachmann, P. Bucksbaum, R. Coffee, F.J. Decker, Y. Ding, D. Dowell, S. Edstrom, A. Fisher, J. Frisch, S. Gilevich, J. Hastings, G. Hays, HeringPh, Z. Huang, R. Iverson, H. Loos, M. Messerschmidt, A. Miahnahri, S. Moeller, H.D. Nuhn, G. Pile, D. Ratner, J. Rzepiela, D. Schultz, T. Smith, P. Stefan,

H. Tompkins, J. Turner, J. Welch, W. White, J. Wu, G. Yocky, J. Galayda, Nat. Photonics **4**, 641 (2010)
11. L. Young, E.P. Kanter, B. Krässig, Y. Li, A.M. March, S.T. Pratt, R. Santra, S.H. Southworth, N. Rohringer, L.F. DiMauro, G. Doumy, C.A. Roedig, N. Berrah, L. Fang, M. Hoener, P.H. Bucksbaum, J.P. Cryan, S. Ghimire, J.M. Glownia, D.A. Reis, J.D. Bozek, C. Bostedt, M. Messerschmidt, Nature **466**, 56 (2010)
12. E.L. Saldin, E.A. Schneidmiller, M.V. Yurkov, Opt. Commun. **239**, 161 (2004)
13. A.A. Zholents, W.M. Fawley, Phys. Rev. Lett. **92**, 224801 (2004)
14. A.A. Zholents, G. Penn, Phys. Rev. ST Accel. Beams **8**, 050704 (2005)
15. E.L. Saldin, E.A. Schneidmiller, M.V. Yurkov, Phys. Rev. ST Accel. Beams **9**, 050702 (2006)
16. M. Nagasono, E. Suljoti, A. Pietzsch, F. Hennies, M. Wellhöfer, J.T. Hoeft, M. Martins, W. Wurth, R. Treusch, J. Feldhaus, J.R. Schneider, A. Föhlisch, Phys. Rev. A **75**, 051406(R) (2007)
17. N.R. Thompson, B.W.J. Mcneil, Phys. Rev. Lett. **100**, 203901 (2008)
18. G. Lambert, T. Hara, D. Garzella, T. Tanikawa, M. Labat, B. Carre, H. Kitamura, T. Shintake, M. Bougeard, S. Inoue, Y. Tanaka, P. Salieres, H. Merdji, O. Chubar, O. Gobert, K. Tahara, M.E. Couprie, Nat. Phys. **4**, 296 (2008)
19. M. Lewenstein, P. Balcou, Ivanov, A. L'Huillier, P.B. Corkum, Phys. Rev. A **49**, 2117 (1994)
20. M.Y. Ivanov, T. Brabec, N. Burnett, Phys. Rev. A **54**, 742 (1996)
21. K.J. Schafer, K.C. Kulander, Phys. Rev. Lett. **78**, 638 (1997)
22. W. Becker, A. Lohr, M. Kleber, M. Lewenstein, Phys. Rev. A **56**, 645 (1997)
23. I.P. Christov, M.M. Murnane, H.C. Kapteyn, Phys. Rev. Lett. **78**, 1251 (1997)
24. M. Drescher, M. Hentschel, R. Kienberger, G. Tempea, C. Spielmann, G.A. Reider, P.B. Corkum, F. Krausz, Science **291**, 1923 (2001)
25. P. Agostini, L.F. Dimauro, Rep. Prog. Phys. **67**, 813 (2004)
26. G. Sansone, E. Benedetti, F. Calegari, C. Vozzi, L. Avaldi, R. Flammini, L. Poletto, P. Villoresi, C. Altucci, R. Velotta, S. Stagira, S. De Silvestri, M. Nisoli, Science **314**, 443 (2006)
27. E. Goulielmakis, M. Schultze, M. Hofstetter, V.S. Yakovlev, J. Gagnon, M. Uiberacker, A.L. Aquila, E.M. Gullikson, D.T. Attwood, R. Kienberger, F. Krausz, U. Kleineberg, Science **320**, 1614 (2008)
28. M.B. Gaarde, J.L. Tate, K.J. Schafer, J. Phys. B **41**, 132001 (2008)
29. E.A. Gibson, A. Paul, N. Wagner, R. Tobey, D. Gaudiosi, S. Backus, I.P. Christov, A. Aquila, E.M. Gullikson, D.T. Attwood, M.M. Murnane, H.C. Kapteyn, Science **302**, 95 (2003)
30. J. Seres, V.S. Yakovlev, E. Seres, C. Streli, P. Wobrauschek, C. Spielmann, F. Krausz, Nat. Phys. **3**, 878 (2007)
31. X. Zhang, A.L. Lytle, T. Popmintchev, X. Zhou, H.C. Kapteyn, M.M. Murnane, O. Cohen, Nat. Phys. **3**, 270 (2007)
32. N.M. Naumova, J.A. Nees, I.V. Sokolov, B. Hou, G.A. Mourou, Phys. Rev. Lett. **92**, 063902 (2004)
33. B. Dromey, M. Zepf, A. Gopal, K. Lancaster, M.S. Wei, K. Krushelnick, M. Tatarakis, N. Vakakis, S. Moustaizis, R. Kodama, M. Tampo, C. Stoeckl, R. Clarke, H. Habara, D. Neely, S. Karsch, P. Norreys, Nat. Phys. **2**, 456 (2006)
34. G.D. Tsakiris, K. Eidmann, J. Meyer-Ter-Vehn, F. Krausz, New J. Phys. **8**, 19 (2006)
35. Y. Nomura, R. Horlein, P. Tzallas, B. Dromey, S. Rykovanov, Z. Major, J. Osterhoff, S. Karsch, L. Veisz, M. Zepf, D. Charalambidis, F. Krausz, G.D. Tsakiris, Nat. Phys. **5**, 124 (2008)
36. B. Dromey, S.G. Rykovanov, D. Adams, R. Hörlein, Y. Nomura, D.C. Carroll, P.S. Foster, S. Kar, K. Markey, P. McKenna, D. Neely, M. Geissler, G.D. Tsakiris, M. Zepf, Phys. Rev. Lett. **102**, 225002 (2009)
37. A. Scrinzi, M.Y. Ivanov, R. Kienberger, D.M. Villeneuve, J. Phys. B **39**, R1 (2006)
38. P.B. Corkum, F. Krausz, Nat. Phys. **3**, 381 (2007)
39. M.F. Kling, M.J.J. Vrakking, Annu. Rev. Phys. Chem. **59**, 463 (2008)
40. P.B. Corkum, Z. Chang, Opt. Photon. News **19**, 24 (2008)
41. F. Krausz, M. Ivanov, Rev. Mod. Phys **81**, 163 (2009)

42. S. Nagele, Interaction of helium with intense ultrashort laser pulses. Master's thesis, TU Wien (2007)
43. R. Pazourek, Electronic correlation effects in helium on the attosecond time scale. Master's thesis, Vienna Univ. of Technology (2008)
44. J. Feist, Two-photon double ionization of helium. Ph.D. thesis, Vienna Univ. of Technology (2009)
45. J. Feist, S. Nagele, R. Pazourek, E. Persson, B.I. Schneider, L.A. Collins, J. Burgdörfer, Phys. Rev. A **77**, 043420 (2008)
46. J. Feist, R. Pazourek, S. Nagele, E. Persson, B.I. Schneider, L.A. Collins, J. Burgdörfer, J. Phys. B **42**, 134014 (2009)
47. J. Feist, S. Nagele, R. Pazourek, E. Persson, B.I. Schneider, L.A. Collins, J. Burgdörfer, Phys. Rev. Lett. **103**, 063002 (2009)
48. J. Feist, R. Pazourek, S. Nagele, E. Persson, B.I. Schneider, L.A. Collins, J. Burgdorfer, J. Phys.: Conf. Ser. **194**, 012010 (2009)
49. M. Kurka, J. Feist, D.A. Horner, A. Rudenko, Y.H. Jiang, K.U. Kühnel, L. Foucar, T.N. Rescigno, C.W. McCurdy, R. Pazourek, S. Nagele, M. Schulz, O. Herrwerth, M. Lezius, M.F. Kling, M. Schöffler, A. Belkacem, S. Düsterer, R. Treusch, B.I. Schneider, L.A. Collins, J. Burgdörfer, C.D. Schröter, R. Moshammer, J. Ullrich, New J. Phys. **12**, 073035 (2010)
50. S.X. Hu, L.A. Collins, B.I. Schneider, Phys. Rev. A **80**, 023426 (2009)
51. F.W. Byron, C.J. Joachain, Phys. Rev. **164**, 1 (1967)
52. T. Åberg, Phys. Rev. A **2**, 1726 (1970)
53. A. Dalgarno, H.R. Sadeghpour, Phys. Rev. A **46**, R3591 (1992)
54. L.R. Andersson, J. Burgdörfer, Phys. Rev. Lett. **71**, 50 (1993)
55. D. Proulx, R. Shakeshaft, Phys. Rev. A **48**, R875 (1993)
56. M. Pont, R. Shakeshaft, Phys. Rev. A **51**, R2676 (1995)
57. M.S. Pindzola, F. Robicheaux, Phys. Rev. A **57**, 318 (1998)
58. Y. Qiu, J.Z. Tang, J. Burgdörfer, J. Wang, Phys. Rev. A **57**, R1489 (1998)
59. D. Dundas, K.T. Taylor, J.S. Parker, E.S. Smyth, J. Phys. B **32**, L231 (1999)
60. A. Becker, F.H.M. Faisal, Phys. Rev. A **59**, R1742 (1999)
61. M. Lein, E.K.U. Gross, V. Engel, Phys. Rev. Lett. **85**, 4707 (2000)
62. J.S. Parker, L.R. Moore, K.J. Meharg, D. Dundas, K.T. Taylor, J. Phys. B **34**, L69 (2001)
63. M.S. Pindzola, F. Robicheaux, J. Phys. B **31**, L823 (1998)
64. M.A. Kornberg, P. Lambropoulos, J. Phys. B **32**, L603 (1999)
65. M.G. Makris, L.A.A. Nikolopoulos, P. Lambropoulos, Europhys. Lett. **54**, 722 (2001)
66. T. Mercouris, C. Haritos, C.A. Nicolaides, J. Phys. B **34**, 3789 (2001)
67. J. Colgan, M.S. Pindzola, F. Robicheaux, J. Phys. B **34**, L457 (2001)
68. L.A.A. Nikolopoulos, P. Lambropoulos, J. Phys. B **34**, 545 (2001)
69. J. Colgan, M.S. Pindzola, Phys. Rev. Lett. **88**, 173002 (2002)
70. T. Nakajima, L.A.A. Nikolopoulos, Phys. Rev. A **66**, 041402 (2002)
71. B. Piraux, J. Bauer, S. Laulan, H. Bachau, Eur. Phys. J. D **26**, 7 (2003)
72. S. Laulan, H. Bachau, Phys. Rev. A **68**, 013409 (2003)
73. L. Feng, H.W. van der Hart, J. Phys. B **36**, L1 (2003)
74. S. Laulan, H. Bachau, Phys. Rev. A **69**, 033408 (2004)
75. K.L. Ishikawa, K. Midorikawa, Phys. Rev. A **72**, 013407 (2005)
76. S.X. Hu, J. Colgan, L.A. Collins, J. Phys. B **38**, L35 (2005)
77. A.S. Kheifets, I.A. Ivanov, J. Phys. B **39**, 1731 (2006)
78. A.Y. Istomin, E.A. Pronin, N.L. Manakov, S.I. Marmo, A.F. Starace, Phys. Rev. Lett. **97**, 123002 (2006)
79. I.F. Barna, J. Wang, J. Burgdörfer, Phys. Rev. A **73**, 023402 (2006)
80. E. Foumouo, G. Lagmago Kamta, G. Edah, B. Piraux, Phys. Rev. A **74**, 063409 (2006)
81. E. Foumouo, Piraux, S. Laulan, H. Bachau, J. Phys. B **39**, S427 (2006)
82. L.A.A. Nikolopoulos, P. Lambropoulos, J. Phys. B **39**, 883 (2006)
83. E.A. Pronin, N.L. Manakov, S.I. Marmo, A.F. Starace, J. Phys. B **40**, 3115 (2007)
84. R. Shakeshaft, Phys. Rev. A **76**, 063405 (2007)
85. A.S. Kheifets, A.I. Ivanov, I. Bray, Phys. Rev. A **75**, 024702 (2007)

86. L.A.A. Nikolopoulos, P. Lambropoulos, J. Phys. B **40**, 1347 (2007)
87. T. Morishita, S. Watanabe, C.D. Lin, Phys. Rev. Lett. **98**, 083003 (2007)
88. I.A. Ivanov, A.S. Kheifets, Phys. Rev. A **75**, 033411 (2007)
89. S.X. Hu, L.A. Collins, Phys. Rev. A **71**, 062707 (2005)
90. S.X. Hu, L.A. Collins, Phys. Rev. Lett. **96**, 073004 (2006)
91. S.X. Hu, L.A. Collins, J. Mod. Opt. **54**, 943 (2007)
92. A.S. Kheifets, I.A. Ivanov, I. Bray, Phys. Rev. A **76**, 025402 (2007)
93. D.A. Horner, F. Morales, T.N. Rescigno, F. Martín, C.W. McCurdy, Phys. Rev. A **76**, 030701(R) (2007)
94. S. Fritzsche, A.N. Grum-Grzhimailo, E.V. Gryzlova, N.M. Kabachnik, J. Phys. B **41**, 165601 (2008)
95. T. Sekikawa, T. Okamoto, E. Haraguchi, M. Yamashita, T. Nakajima, Opt. Express **16**, 21922 (2008)
96. B. Piraux, E. Foumouo, P. Antoine, H. Bachau, J. Phys.: Conf. Ser. **141**, 012013 (2008)
97. P. Lambropoulos, L.A.A. Nikolopoulos, M.G. Makris, A. Mihelic, Phys. Rev. A **78**, 055402 (2008)
98. D.A. Horner, C.W. McCurdy, T.N. Rescigno, Phys. Rev. A **78**, 043416 (2008)
99. P. Antoine, E. Foumouo, B. Piraux, T. Shimizu, H. Hasegawa, Y. Nabekawa, K. Midorikawa, Phys. Rev. A **78**, 023415 (2008)
100. X. Guan, K. Bartschat, B.I. Schneider, Phys. Rev. A **77**, 043421 (2008)
101. D.A. Horner, T.N. Rescigno, C.W. McCurdy, Phys. Rev. A **77**, 030703(R) (2008)
102. A. Palacios, T.N. Rescigno, C.W. McCurdy, Phys. Rev. A **77**, 032716 (2008)
103. P. Lambropoulos, L.A.A. Nikolopoulos, New J. Phys. **10**, 025012 (2008)
104. E. Foumouo, P. Antoine, H. Bachau, B. Piraux, New J. Phys. **10**, 025017 (2008)
105. E. Foumouo, P. Antoine, B. Piraux, L. Malegat, H. Bachau, R. Shakeshaft, J. Phys. B **41**, 051001 (2008)
106. A. Palacios, T.N. Rescigno, C.W. McCurdy, Phys. Rev. A **79**, 033402 (2009)
107. I.A. Ivanov, A.S. Kheifets, Phys. Rev. A **79**, 023409 (2009)
108. T.G. Lee, M.S. Pindzola, F. Robicheaux, Phys. Rev. A **79**, 053420 (2009)
109. Y. Nabekawa, H. Hasegawa, E.J. Takahashi, K. Midorikawa, Phys. Rev. Lett. **94**, 043001 (2005)
110. H. Hasegawa, E.J. Takahashi, Y. Nabekawa, K.L. Ishikawa, K. Midorikawa, Phys. Rev. A **71**, 023407 (2005)
111. A.A. Sorokin, M. Wellhofer, S.V. Bobashev, K. Tiedtke, M. Richter, Phys. Rev. A **75**, 051402(R) (2007)
112. A. Rudenko, L. Foucar, M. Kurka, T. Ergler, K.U. Kühnel, Y.H. Jiang, A. Voitkiv, B. Najjari, A. Kheifets, S. Lüdemann, T. Havermeier, M. Smolarski, S. Schössler, K. Cole, M. Schöffler, R. Dörner, S. Düsterer, W. Li, B. Keitel, R. Treusch, M. Gensch, C.D. Schröter, R. Moshammer, J. Ullrich, Phys. Rev. Lett. **101**, 073003 (2008)
113. A. Palacios, T.N. Rescigno, C.W. McCurdy, Phys. Rev. Lett. **103**, 253001 (2009)
114. E. Foumouo, A. Hamido, P. Antoine, B. Piraux, H. Bachau, R. Shakeshaft, J. Phys. B **43**, 091001 (2010)
115. T.N. Rescigno, C.W. McCurdy, Phys. Rev. A **62**, 032706 (2000)
116. C.W. McCurdy, D.A. Horner, T.N. Rescigno, Phys. Rev. A **63**, 022711 (2001)
117. B.I. Schneider, L.A. Collins, J. Non-Cryst. Solids **351**, 1551 (2005)
118. B.I. Schneider, L.A. Collins, S.X. Hu, Phys. Rev. E **73**, 036708 (2006)
119. A. Scrinzi, N. Elander, J. Chem. Phys. **98**, 3866 (1993)
120. R.L.R. Mohan, *Finite Element and Boundary Element Applications in Quantum Mechanics* (Oxford University Press, 2002)
121. W. Schweizer, *Numerical Quantum Dynamics* (Springer, 2001)
122. J.V. Lill, G.A. Parker, J.C. Light, Chem. Phys. Lett. **89**, 483 (1982)
123. J.C. Light, I.P. Hamilton, J.V. Lill, J. Chem. Phys. **82**, 1400 (1985)
124. J.V. Lill, G.A. Parker, J.C. Light, J. Chem. Phys. **85**, 900 (1986)
125. G.C. Corey, J.W. Tromp, J. Chem. Phys. **103**, 1812 (1995)
126. A.S. Dickinson, P.R. Certain, J. Chem. Phys. **49**, 4209 (1968)

127. G. Szegö, *Orthogonal Polynomials* (American Mathematical Society, 1975)
128. D. Baye, P.H. Heenen, J. Phys. A **19**, 2041 (1986)
129. D. Baye, M. Hesse, M. Vincke, Phys. Rev. E **65**, 026701 (2002)
130. D. Baye, Phys. Status. Solidi B **243**, 1095 (2006)
131. J.C. Light, T. Carrington, Adv. Chem. Phys **114**, 263 (2000)
132. C. Leforestier, R.H. Bisseling, C. Cerjan, M.D. Feit, R. Friesner, A. Guldberg, A. Hammerich, G. Jolicard, W. Karrlein, H.D. Meyer, N. Lipkin, O. Roncero, R. Kosloff, J. Comp. Phys. **94**, 59 (1991)
133. C. Lanczos, J. Res. Nat. Bur. Standards **45**, 255 (1950)
134. W.E. Arnoldi, Q. Appl. Math. **9**, 17 (1951)
135. H. De Raedt, Comput. Phys. Rep. **7**, 1 (1987)
136. F. He, C. Ruiz, A. Becker. Absorbing boundaries in numerical solutions of the time-dependent schrödinger equation. arXiv:physics/0701265 (2007). Physics/0701265v1
137. U.V. Riss, H.D. Meyer, J. Phys. B **28**, 1475 (1995)
138. M.S. Pindzola, D.R. Schultz, Phys. Rev. A **53**, 1525 (1996)
139. M.S. Pindzola, F. Robicheaux, Phys. Rev. A **54**, 2142 (1996)
140. C.W. McCurdy, M. Baertschy, T.N. Rescigno, J. Phys. B **37**, R137 (2004)
141. H.S. Friedrich, *Theoretical Atomic Physics* (Springer, Berlin, 2005)
142. G. Breit, H.A. Bethe, Phys. Rev. **93**, 888 (1954)
143. S. Altshuler, Il Nuovo Cimento **3**, 246 (1956)
144. R. Szmytkowski, M. Gruchowski, J. Quant. Spectrosc. Radiat. Transfer **94**, 127 (2005)
145. J. Berakdar, J.S. Briggs, Phys. Rev. Lett. **72**, 3799 (1994)
146. F. Maulbetsch, J.S. Briggs, J. Phys. B **26**, 1679 (1993)
147. C.W. McCurdy, F. Martín, J. Phys. B **37**, 917 (2004)
148. P.L. Bartlett, J. Phys. B **39**, R379 (2006)
149. G.F. Gribakin, V.K. Ivanov, A.V. Korol, Y.M. Kuchiev, J. Phys. B **32**, 5463 (1999)
150. R. Nepstad, T. Birkeland, M. Førre, Phys. Rev. A **81**, 063402 (2010)
151. T.A. Carlson, Phys. Rev. **156**, 142 (1967)
152. G.H. Wannier, Phys. Rev. **90**, 817 (1953)
153. R. Wehlitz, F. Heiser, O. Hemmers, B. Langer, A. Menzel, U. Becker, Phys. Rev. Lett. **67**, 3764 (1991)
154. H. Bräuning, R. Dörner, C.L. Cocke, M.H. Prior, B. Krässig, A.S. Kheifets, I. Bray, A. Bräuning-Demian, K. Carnes, S. Dreuil, V. Mergel, P. Richard, J. Ullrich, H. Schmidt-Böcking, J. Phys. B **31**, 5149 (1998)
155. S. Cvejanovic, F.H. Read, J. Phys. B **7**, 1841 (1974)
156. G. Tanner, K. Richter, J.M. Rost, Rev. Mod. Phys **72**, 497 (2000)
157. G. Gerber, R. Morgenstern, A. Niehaus, J. Phys. B **5**, 1396 (1972)
158. A. Russek, W. Mehlhorn, J. Phys. B **19**, 911 (1986)
159. G.B. Armen, J. Tulkki, T. Åberg, B. Crasemann, Phys. Rev. A **36**, 5606 (1987)
160. R.B. Barker, H.W. Berry, Phys. Rev. **151**, 14 (1966)
161. M.J.J. Vrakking, Physics **2**, 72 (2009)
162. A. Staudte, S. Patchkovskii, D. Pavičić, H. Akagi, O. Smirnova, D. Zeidler, M. Meckel, D.M. Villeneuve, R. Dörner, Yu, P.B. Corkum, Phys. Rev. Lett. **102**, 033004 (2009)
163. M. Magrakvelidze, F. He, S. De, I. Bocharova, D. Ray, U. Thumm, I.V. Litvinyuk, Phys. Rev. A **79**, 033408 (2009)
164. H.D. Cohen, U. Fano, Phys. Rev. **150**, 30 (1966)
165. M. Walter, J. Briggs, J. Phys. B **32**, 2487 (1999)
166. J. Fernández, O. Fojón, A. Palacios, F. Martín, Phys. Rev. Lett. **98**, 043005 (2007)
167. D.A. Horner, S. Miyabe, T.N. Rescigno, C.W. McCurdy, F. Morales, F. Martín, Phys. Rev. Lett. **101**, 183002 (2008)
168. D. Rolles, M. Braune, S. Cvejanovic, O. Geszner, R. Hentges, S. Korica, B. Langer, T. Lischke, G. Prumper, A. Reinkoster, J. Viefhaus, B. Zimmermann, V. McKoy, U. Becker, Nature **437**, 711 (2005)